



NAVAL POSTGRADUATE SCHOOL

MONTEREY, CALIFORNIA

THESIS

**THE EFFECT OF SENSITIZATION ON THE STRESS
CORROSION CRACKING OF ALUMINUM ALLOY 5456**

by

Emily C. Cormack

June 2012

Thesis Advisor:
Second Reader:

Luke N. Brewer
Joseph C. Farmer

Approved for public release; distribution is unlimited

THIS PAGE INTENTIONALLY LEFT BLANK

REPORT DOCUMENTATION PAGE			<i>Form Approved OMB No. 0704-0188</i>	
Public reporting burden for this collection of information is estimated to average 1 hour per response, including the time for reviewing instruction, searching existing data sources, gathering and maintaining the data needed, and completing and reviewing the collection of information. Send comments regarding this burden estimate or any other aspect of this collection of information, including suggestions for reducing this burden, to Washington headquarters Services, Directorate for Information Operations and Reports, 1215 Jefferson Davis Highway, Suite 1204, Arlington, VA 22202-4302, and to the Office of Management and Budget, Paperwork Reduction Project (0704-0188) Washington DC 20503.				
1. AGENCY USE ONLY (Leave blank)		2. REPORT DATE June 2012	3. REPORT TYPE AND DATES COVERED Master's Thesis	
4. TITLE AND SUBTITLE The Effect of Sensitization on the Stress Corrosion Cracking of Aluminum Alloy 5456			5. FUNDING NUMBERS	
6. AUTHOR(S) Emily C. Cormack				
7. PERFORMING ORGANIZATION NAME(S) AND ADDRESS(ES) Naval Postgraduate School Monterey, CA 93943-5000			8. PERFORMING ORGANIZATION REPORT NUMBER	
9. SPONSORING /MONITORING AGENCY NAME(S) AND ADDRESS(ES) N/A			10. SPONSORING/MONITORING AGENCY REPORT NUMBER	
11. SUPPLEMENTARY NOTES The views expressed in this thesis are those of the author and do not reflect the official policy or position of the Department of Defense or the U.S. Government. IRB Protocol number _____N/A_____.				
12a. DISTRIBUTION / AVAILABILITY STATEMENT Approved for public release; distribution is unlimited			12b. DISTRIBUTION CODE A	
13. ABSTRACT (maximum 200 words) This work examines the effect of sensitization on the stress corrosion cracking behavior of marine grade aluminum alloys (Al-Mg). These alloys can be sensitized during operation, promoting their susceptibility to intergranular stress corrosion cracking (IGSCC). Aluminum alloy 5456-H116 (also identified as Al-Mg5.1) samples were sensitized at 175°C for varying durations of time and then mechanically tested in salt water. Mass loss tests quantified the degree of sensitization (DOS) as a function of sensitization time. Dual cantilever beam tests were used to measure the SCC growth rate and cyclic fatigue tests were conducted to determine the corrosion fatigue behavior. DOS increased as sensitization time increased with little difference in mass losses above 336 hours. Stress corrosion crack growth rate increased as sensitization time increased. Although the sensitization rates for AA5456-H116 were higher than for AA5083, the stress corrosion crack growth rates were significantly lower. The stress corrosion fracture surfaces showed clear showed a clearly intergranular fracture path with extensive crack branching and delamination in the transverse direction.				
14. SUBJECT TERMS Stress Corrosion Cracking, 5456 Aluminum Alloy			15. NUMBER OF PAGES 101	
			16. PRICE CODE	
17. SECURITY CLASSIFICATION OF REPORT Unclassified	18. SECURITY CLASSIFICATION OF THIS PAGE Unclassified	19. SECURITY CLASSIFICATION OF ABSTRACT Unclassified	20. LIMITATION OF ABSTRACT UU	

NSN 7540-01-280-5500

Standard Form 298 (Rev. 2-89)
Prescribed by ANSI Std. Z39-18

THIS PAGE INTENTIONALLY LEFT BLANK

Approved for public release; distribution is unlimited

**THE EFFECT OF SENSITIZATION ON THE STRESS CORROSION
CRACKING OF ALUMINUM ALLOY 5456**

Emily C. Cormack
Lieutenant, United States Navy
B.S., United States Naval Academy, 2008

Submitted in partial fulfillment of the
requirements for the degree of

MASTER OF SCIENCE IN MECHANICAL ENGINEERING

from the

**NAVAL POSTGRADUATE SCHOOL
June 2012**

Author: Emily C. Cormack

Approved by: Luke N. Brewer
Thesis Advisor

Joseph C. Farmer
Second Reader

Knox Millsaps
Chair, Department of Mechanical and Aerospace Engineering

THIS PAGE INTENTIONALLY LEFT BLANK

ABSTRACT

This work examines the effect of sensitization on the stress corrosion cracking behavior of marine grade aluminum alloys (Al-Mg). These alloys can be sensitized during operation, promoting their susceptibility to intergranular stress corrosion cracking (IGSCC). Aluminum alloy 5456-H116 (also identified as Al-Mg5.1) samples were sensitized at 175°C for varying durations of time and then mechanically tested in salt water. Mass loss tests quantified the degree of sensitization (DOS) as a function of sensitization time. Dual cantilever beam tests were used to measure the SCC growth rate and cyclic fatigue tests were conducted to determine the corrosion fatigue behavior. DOS increased as sensitization time increased with little difference in mass losses above 336 hours. Stress corrosion crack growth rate increased as sensitization time increased. Although the sensitization rates for AA5456-H116 were higher than for AA5083, the stress corrosion crack growth rates were significantly lower. The stress corrosion fracture surfaces showed clear showed a clearly intergranular fracture path with extensive crack branching and delamination in the transverse direction.

THIS PAGE INTENTIONALLY LEFT BLANK

TABLE OF CONTENTS

I.	INTRODUCTION AND BACKGROUND.....	1
A.	MOTIVATION	1
1.	Aluminum – Corrosion Resistance and Strength	1
2.	Stress Corrosion Cracking in the Fleet.....	5
B.	INTRODUCTION.....	7
1.	Stress Corrosion Cracking	8
2.	Stress Corrosion Crack Propagation	15
3.	Stress Corrosion Cracking Mechanisms.....	16
4.	Corrosion Fatigue	24
5.	Mitigating Stress Corrosion Cracking and Corrosion Fatigue	30
C.	THESIS OBJECTIVES.....	32
II.	EXPERIMENTAL PROCEDURE.....	35
A.	MATERIAL PROCESSING	35
1.	Plate Fabrication.....	35
2.	Sample Sensitization and Preparation.....	37
B.	STRESS CORROSION CRACKING – DUAL CANTILEVER BEAM (DCB)	38
1.	Sample Geometry.....	38
2.	Pre-cracking	38
3.	SCC Static Loading Test	40
C.	CORROSION FATIGUE – SINGLE EDGE NOTCH BEAM (SENB) ...	44
1.	Sample Geometry.....	44
2.	Pre-cracking	45
3.	Increasing ΔK to Determine Threshold	45
D.	NITRIC ACID MASS LOSS TEST – ASTM G67.....	47
E.	MICROSTRUCTURAL ANALYSIS	47
1.	Fracture Surface Characterization	47
2.	Crack Surface Characterization.....	48
F.	HARDNESS MEASUREMENTS.....	49
1.	Hardness Tests	49
III.	RESULTS AND DISCUSSION	51
A.	MASS LOSS TEST (ASTM G67).....	51
1.	Mass Loss Results	51
2.	Mass Loss Comparison with AA5083	53
B.	HARDNESS.....	56
1.	Rockwell B Hardness Results	56
2.	Comparison with AA5456-H116 Hardness in Literature	58
C.	STRESS CORROSION CRACKING.....	60
1.	DCB Constant Displacement SCC Crack Growth Rate Test Results	60
2.	AA5456-H116 Crack Growth Rate Comparison with AA5083	62

C.	CORROSION FATIGUE ΔK_{TH} DETERMINATION	63
1.	SENB Corrosion Fatigue Results	63
D.	MICROSTRUCTURAL ANALYSIS	65
1.	SCC Propagation Mode in DCB Samples.....	65
2.	Comparison of Fracture Surfaces with AA5083	70
F.	FUTURE WORK	71
IV.	CONCLUSIONS	75
	LIST OF REFERENCES	77
	INITIAL DISTRIBUTION LIST	81

LIST OF FIGURES

Figure 1.	Effect of pH on corrosion rate of aluminum. a. acetic acid; b. hydrochloric acid; c. hydrofluoric acid; d. nitric acid; e. phosphoric acid; f. sulfuric acid; g. ammonium hydroxide; h. sodium carbonate; i. sodium disilicate; j. sodium hydroxide. (From Hatch, [4])	3
Figure 2.	Phase Diagram for Al-Mg (From ASM International, [6]).....	4
Figure 3.	Schematic showing how intergranular stress corrosion cracking occurs in sensitized Al-Mg material.....	4
Figure 4.	AA5456-H116 Direct weather exposed deck-plate displaying stress corrosion cracking. (From Schwarting et al. [5]).....	6
Figure 5.	AA5456-H116 Interior structure exposed to conductive heat and corrosive humid environment. (From Schwarting et al. [5])	6
Figure 6.	Venn Diagram showing the mutual importance of Sensitization, Tensile Stress and Corrosive Environment on SCC.....	9
Figure 7.	Effect of sensitization temperature and time on IGC susceptibility of AA5083-H116. (From Oguocha et al. [19])	11
Figure 8.	Microstructure Evolution of AA5083 at 175°C. (From Holtz et al. [12])	11
Figure 9.	Increases in Mass Loss in ASTM G67 Correspond to Increases in S-L DCB Crack Growth Rates. Data converted to metric units. (From Bovard, [13]).....	12
Figure 10.	Increases in Mass Loss in ASTM G67 Correspond to Increases in S-L DCB Crack Growth Rates at Various Stress Intensity Factors. Data converted to metric units. (From Bovard, [13]).....	13
Figure 11.	Comparison of SEM fractograph of (A) as-received 5456-H116 and (B) 5456-H116 exposed to 175°C for 100 h. There was significant delamination in (B), while none was exhibited in (A). (From Brosi et al. [14]).....	14
Figure 12.	Intergranular corrosion starting on the surface of AA5083. (From Scully et al.[21]).....	15
Figure 13.	Pourbaix diagram for aluminum showing corrosion, passivation, and immunity regions as a function of pH and potential. Chemical reactions for separation lines are indicated. (From Pourbaix, [27]).....	21
Figure 14.	Schematic representation of crack propagation by the film-rupture model. (a) Crack tip stays bare as a result of continuous deformation. (b) Crack tip passivates and is ruptures repeatedly. (From Farmer, [29]).....	21
Figure 15.	Schematic showing possible crack-tip/particle interactions for electrochemically active particles. (From Jones, [26])	23
Figure 16.	Illustration of corrosion tunnel model. (a) Schematic of tunnel model showing the initiation of a crack by the formation of corrosion tunnels at slip steps and ductile deformation and fracture of the remaining ligaments. (b) Schematic diagram of the tunnel mechanism of SCC and flat slot formation. (From Jones, [30]).....	24

Figure 17.	Stress amplitude (S) versus logarithm of the number of cycles to fatigue failure (N) comparison between steel that does have a fatigue limit and aluminum that does not have a fatigue limit. (From Schwarting et al. [5]).....	25
Figure 18.	Schematic illustration of the different regimes of stable fatigue crack propagation. (From McEvily, [33])	27
Figure 19.	da/dN for R = 0.1 in Air, Vacuum, and Saltwater for As Received (R) and Sensitized (S) Samples. (From Holtz et al. [12])	29
Figure 20.	da/dN for R = 0.85 in Air, Vacuum, and Saltwater for As Received (R) and Sensitized (S) Samples. (From Holtz et al. [12])	30
Figure 21.	An S-N curve comparing the fatigue limit increases of 7075-T7351 aluminum alloy from shot peening and laser peening. (From Montross et al.[41]).....	32
Figure 22.	Double Cantilever Beam Test Specimen with ruler in inches	35
Figure 23.	Single Edge Notch Beam Test Specimen with ruler in inches	36
Figure 24.	Specimen Orientation: DCB samples were fabricated in the S-L orientation and SENB were fabricated in the T-L orientation. (From ASTM E399, [43])	36
Figure 25.	Detailed view of Chevron notch crack starter with dimensions provided in inches	37
Figure 26.	Top and side view of the plane strain DCB sample with dimensions provided in inches.	38
Figure 27.	MTS 858 Machine	39
Figure 28.	Detailed view of double cantilever beam pre-cracking setup in MTS.....	39
Figure 29.	Type 316 Stainless Steel bolts, 3/8" (9.525 mm) in diameter with 24 TPI (0.98 threads per millimeter) used for static loading of DCB samples.....	41
Figure 30.	Illustration of measurements used to determine the notch mouth opening desired to facilitate SCC	42
Figure 31.	Illustration of NaCl solution drop-wise application to double cantilever beam samples during constant loading test.....	43
Figure 32.	Top and side view of the plane strain SENB sample with measurements provided in inches.	44
Figure 33.	MTS 858 three point bend configuration used for SENB fatigue pre-cracking.....	45
Figure 34.	Tank used for submersion of SENB in three point bend corrosion fatigue tests conducted in 3.5 wt% NaCl	46
Figure 35.	Orientation of sensitized and as received DCB sample Rockwell B hardness tests.	49
Figure 36.	Nitric Acid Mass Loss Test (ASTM G67) for AA5456-H116 showing mass loss as a function of sensitization time.	52
Figure 37.	NAMLT for as received and sensitized samples showing a difference in color between the two. Samples are 1 inch on each side.	52
Figure 38.	Surface flakes and exfoliation present on AA5456-H116 sample sensitized for 336 hour and subject to ASTM G67, nitric acid mass loss test. Sample is 1 inch on each side.	53

Figure 39.	ASTM G67 NAMLT results showing mass loss for AA5083-H131 as a function of aging time and temperature. (From Holtz et al. [12])	54
Figure 40.	ASTM G67 NAMLT results for AA5083-H116. (From Oguocha et al. [19]).....	55
Figure 41.	Assessment on existing base material weldability as a function of mass loss. (From Wong, [44]).....	55
Figure 42.	Effect of sensitization on Rockwell B hardness of AA5456-H116	57
Figure 43.	Effect of thermal conditions on Rockwell B hardness on AA5456-H116 relative to rolling direction.....	58
Figure 44.	Effect of thermal conditions on Rockwell B hardness on AA5456-H116. (From Brosi et al.[14])	59
Figure 45.	Vickers hardness measurements as a function of sensitization time for AA5083-H116. (From Oguocha et al. [19])	59
Figure 46.	Data for measured crack length in millimeters versus time in hours for AA5456-H116.....	60
Figure 47.	Final stress corrosion crack length measurement locations for DCB samples.....	61
Figure 48.	Calculated data for crack velocity in mm/hr versus K_I for AA5456-H116	62
Figure 49.	da/dN data collected on as received AA5456 sample at Fracture Technology Associates	64
Figure 50.	Fatigue of AA5083 in 1% NaCl, Air, and Vacuum of samples sensitized at 175°C for 200 hours and in as received condition with $R = 0.1$. (From Holtz et al. [12]).....	65
Figure 51.	Crack Propagation modes in statically loaded DCB samples subject to SCC with varying mass losses due to sensitization. a) As received (0 mg/cm ²) b) 30mg/cm ² c) 62 mg/cm ²	66
Figure 52.	Secondary Cracks in AA5456-H116 DCB Samples with a mass loss of 63 mg/cm ² after being subjected to static bolt loaded SCC test	67
Figure 53.	SEM images depicting SCC crack initiation characteristics for a statically loaded DCB sample of the as received material with 0 mg/cm ² mass loss. The red arrow indicates a magnified image of the small stress corrosion cracks observed.....	69
Figure 54.	SEM image depicting SCC crack front characteristics for a statically loaded DCB sample aged at 175°C for 24 hours with a mass loss of 30 mg/cm ² and arrow indentifying a crack front indicative of the corrosion tunnel model for SCC propagation.	69
Figure 55.	SEM image depicting SCC crack front characteristics for a statically loaded DCB sample aged at 175°C for 336 hours with a mass loss of 63 mg/cm ² and arrow indicating the presence of two dimensional crack.....	70
Figure 56.	Secondary Cracks in SCC fracture surface for AA5083. (From Bovard,[20]).....	71
Figure 57.	Relationship between ΔK_{th} and K_{ISCC} as a function of mass loss for AA5456. (From Holtz et al. [12])	72

THIS PAGE INTENTIONALLY LEFT BLANK

LIST OF TABLES

Table 1.	Comparison of composition and mechanical properties of several 5xxx series aluminums. (From Kaufman, [11]).....	7
Table 2.	Comparison of K_{ISCC} and ΔK_{th} values for AA5456 and AA5083 from literature. (From Holtz et al. [12]; Bovard et al. [13]; Brosi et al. [14]; and Menzemer et al. [15]; Crane [16])	8
Table 3.	Corrosion potentials for intermetallic compounds common in aluminum alloys. (From Birbilis, [24])	17
Table 4.	Time to Failure for various types of environmental exposure. (From Bovard, [13]).....	20
Table 5.	Summary of mean and amplitude loads used for ΔK threshold corrosion fatigue tests.	46
Table 6.	Grinding and Polishing Conditions.....	49
Table 7.	Mass loss of as received and sensitized AA5456-H116 after ASTM G67 nitric acid mass loss test.....	51

THIS PAGE INTENTIONALLY LEFT BLANK

LIST OF ACRONYMS AND ABBREVIATIONS

SCC	Stress Corrosion Cracking
DoD	Department of Defense
LP	Laser Peening
AA5456	Aluminum Alloy 5456 H116
MIC	Metal Improvement Company
Mg	Magnesium
ICG	Intergranular Corrosion
IGSCC	Intergranular Stress Corrosion Cracking
K_{ISCC}	Threshold Stress Intensity Factor for Stress Corrosion Cracking
USCG	United States Coast Guard
DCB	Double Cantilever Beams
K_{IC}	Plain Strain Fracture Toughness
K_{th}	Threshold Stress Intensity Factor
ST	Short Transverse
LT	Longitudinal Transverse
ALCOA	Aluminum Company of America
% wt	Weight Percent

THIS PAGE INTENTIONALLY LEFT BLANK

ACKNOWLEDGMENTS

I would like to thank Professor Brewer for his unyielding support and continuous fervor for science and the betterment of his students. I have learned a lot about aluminum and stress corrosion cracking and without his encouragement and leadership, this research would have been a lot less enriching.

Dr. Farmer's knowledge of corrosion and dedication to teaching his students is unparalleled and without his guidance, this thesis would have been a lot less complete.

The technical expertise of Mike Nelson at Full Spectrum Machining Inc. and Francine Bovard at Alcoa International helped to make this research both effective and edifying.

I would like to thank the professors and staff of NPS who shared their time and knowledge, especially Dr. C. Park, Dr. S. Menon, and John Mobley.

Finally I would like to thank CDR Baker for both his mentorship and academic proficiency.

THIS PAGE INTENTIONALLY LEFT BLANK

I. INTRODUCTION AND BACKGROUND

A. MOTIVATION

Between the highly competitive field of commercial shipping and the expanding uses of the naval military force, there is a need to increase marine vessel efficiency. Rising fuel costs and the requirement to carry larger loads over greater distances is the chief motivation for improving ship design and construction. Specifically, advancements in the design and fabrication of the new Littoral Combat Ship were completed with an emphasis on the optimization of speed, mission flexibility and shallow draft. One such way to improve ship design is decreasing the weight of building materials in marine vessels while maintaining the strength of the materials currently in use. This conundrum has resulted in the research and development of materials with high strength, low weight, good weldability, and good corrosion resistance for marine and military applications. Aluminum is approximately one third the density of steel with comparable strength and weldability, making it a viable material choice. Specifically, the 5xxx series aluminum alloys have been considered a good choice for marine applications due to their high general corrosion resistance compared to other aluminum alloys.

1. Aluminum – Corrosion Resistance and Strength

The initial choice of using an aluminum alloy for marine applications is due to the fact that in fresh water (with a pH of 4.0 to 8.5) aluminum naturally forms a protective, passivating oxide film illustrated in Figure 1. This film forms on the surface of the material and when damaged, quickly repairs itself for nearly continuous protection of the metal. Using Mg to solid solution strengthen 5xxx series aluminums results in a strong yet light weight material with general corrosion resistance. Aluminum alloys are considered to be “marine grade” when they are of either the H116 or H321 temper and meet the specifications set forth in ASTM Standard B928, the Standard Specification for High Magnesium Aluminum-Alloy Sheet and Plate for Marine Service and Similar Environments [1]. Alloy of the H temper are strain hardened alloys that are not heat

treatable but instead have their strength increased through strain hardening at room temperature. The specific tempers for marine grade certification are defined by the Aluminum Association:

The H116 temper Applies to products manufactured from alloys in the 5xxx series, for which the magnesium content is 3% nominal or more. Products are normally strain hardened at the last operation to specified stable tensile property limits and meet specified levels of corrosion resistance in accelerated type corrosion tests. They are suitable for continuous service at temperatures no greater than 150°F (66°C). Corrosion tests include inter-granular and exfoliation [2].

The H321 temper applies to products from alloys in the 5xxx series, for which the magnesium content is 3% nominal or more. Products are normally thermally stabilized at the last operation to specified stable tensile property limits and meet specified levels of corrosion resistance in accelerated type corrosion tests. They are suitable for continuous service at temperatures no greater than 150°F (66°C). Corrosion tests include inter-granular and exfoliation[2].

For corrosion to occur in these alloys there must be continuous surface damage to the protective oxide film or, the environment must be such that the oxide film becomes permanently degraded. Salt water, with a typical composition of 3.5% NaCl can create an environment that permanently degrades the oxide film by combining the negative Cl^- ions with the positive Al^{3+} ions [3]. This reaction creates holes in the oxide film, ultimately resulting in the corrosion of the aluminum alloys. If the microstructure of the material does not deviate from that formed during the H116 or H321 tempers, then the passivating oxide is stable in most marine environments.

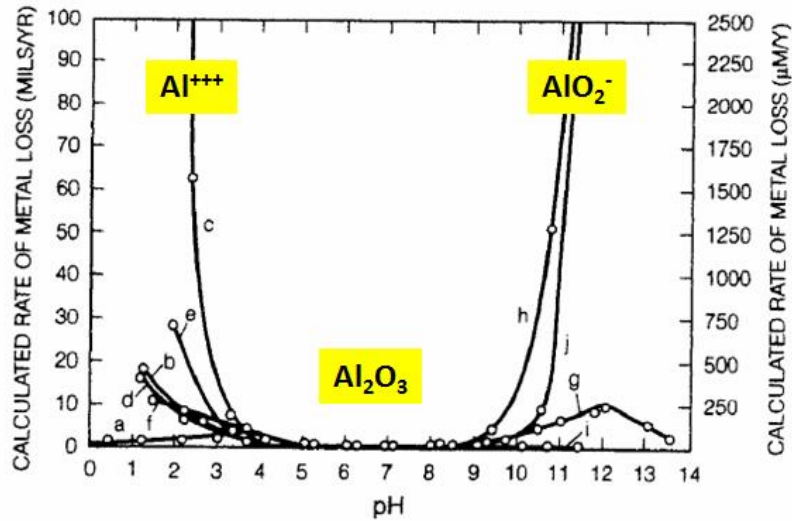


Figure 1. Effect of pH on corrosion rate of aluminum. a. acetic acid; b. hydrochloric acid; c. hydrofluoric acid; d. nitric acid; e. phosphoric acid; f. sulfuric acid; g. ammonium hydroxide; h. sodium carbonate; i. sodium disilicate; j. sodium hydroxide. (From Hatch, [4])

Aluminum alloy 5456 (AA5456) is a great example of the advantages, and possibly crippling disadvantages, of the 5xxx aluminum alloy series. AA5456, which was developed in 1956, is currently in use on above deck structures on many marine vessels, including the U.S. Navy TICONDEROGA (CG-47) class cruisers[5]. Although light weight, sufficiently strong, and easily weldable, AA5456 and other 5xxx series aluminum alloys have presented a strong susceptibility to stress corrosion cracking. The alloying element in this material is magnesium (Mg), which when in solid solution increases the overall strength of the material. However, when an aluminum alloy contains greater than 3 wt% Mg, as is the case with AA5456 (5.1wt%), and is exposed to temperatures above 50°C over the course of many years, the Mg comes out of solid solution resulting in the grain boundary precipitation of a β phase (Mg_2Al_3). Using the phase diagram in Figure 2, the precipitation of the Al_2Mg_3 β -phase at 175°C is expected. Equilibrium leaves 2.8 wt% Mg in AA5083 compared to the 3.2 wt% Mg in AA5456. After the material undergoes this transformation, it is classified as 'sensitized'. Sensitization can occur either during plate fabrication or while in service and results in a material that is susceptible to intergranular stress corrosion cracking (IGSCC), or just SCC.

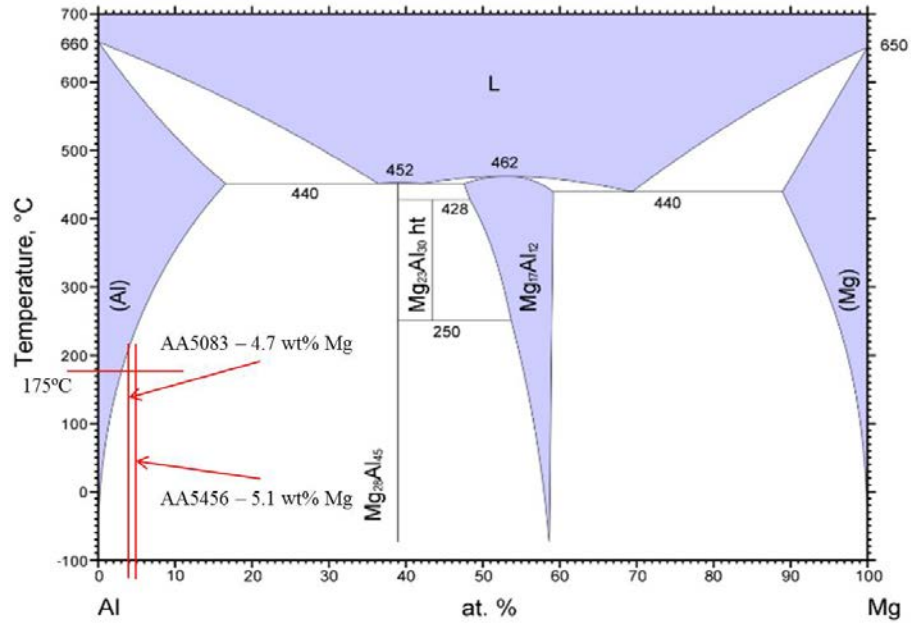


Figure 2. Phase Diagram for Al-Mg (From ASM International, [6])

Two more conditions are required for SCC to take place, a corrosive environment and a tensile stress. When sensitized 5xxx series aluminum is exposed to a corrosive environment, the β phase at the grain boundaries preferentially corrodes and the addition of a tensile stress results in intergranular stress corrosion cracking (IGSCC), shown in Figure 3.

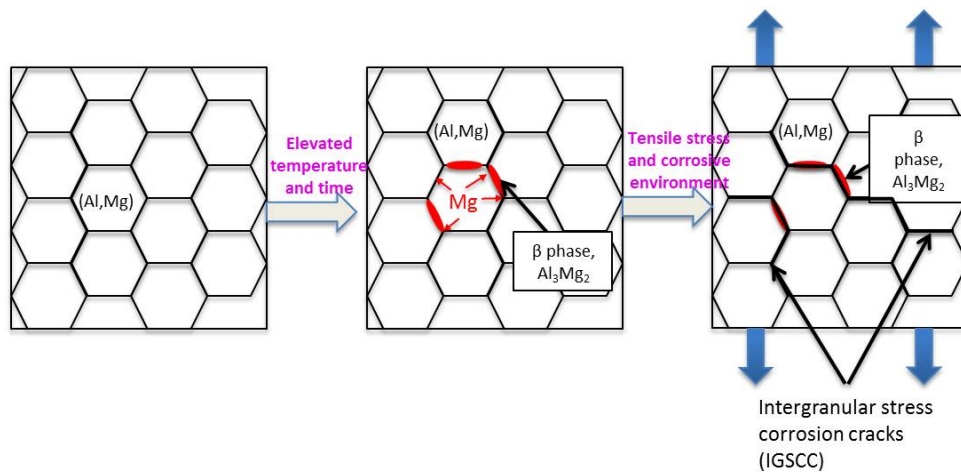


Figure 3. Schematic showing how intergranular stress corrosion cracking occurs in sensitized Al-Mg material.

2. Stress Corrosion Cracking in the Fleet

Intergranular stress corrosion cracking has created a series of expensive repair problems in both the commercial and naval fleets. Between 2001–2002, over 400 commercial marine vessels that were constructed from AA5083, were found to have experienced severe pitting and stress corrosion cracking [7]. These vessels were all built with a single batch of AA5083-H321 plate; an observation that spawned the formation of an Aluminum Solutions Team overseen by the United States Coast Guard (USCG). The final outcome of the investigation team was a letter from the USCG Officer in Charge, Marine Inspection MSO Puget Sound, asking The Aluminum Association Inc. for help in “finding effective long term solutions that clearly identify proper aluminum application in marine vessel repairs and new construction” [7]. The Aluminum Association Inc. responded with the formulation of ASTM-B928, a new national standard for classifying aluminum alloys with high magnesium content to include required corrosion resistance constraints [1]. Previously ASTM-B209 was the standard specification for aluminum and aluminum-alloy sheet and plate, however this standard did not require intergranular corrosion testing, rendering it inadequate for the marine service [8]. While ASTM-B928 is an improvement over previous standards, it is designed to qualify new material used for new ship construction or repair. It does not speak to the sensitization and IGSCC on marine vessels after years of service exposure.

Likewise, IGSCC is plaguing the military marine fleet, mainly the 44 strong TICONDEROGA (CG-47) cruiser class. Early in their lifecycle, all of these ships experienced topside fatigue cracking amidships, due to high localized stresses as well as cyclic loading leading to fatigue and corrosion fatigue [5]. The structural fatigue cracks were identified in the same locations on these ships and were systemically repaired on all 44 cruisers by mitigating the level of fatigue loading in those structures. More recently, many cracks were found forming on the AA5456 superstructures in areas that did not have obvious stress concentrations [5]. Sensitization testing (ASTM G67 [9]) revealed that the material had been sensitized during many years of service at seemingly low temperatures and that cracks had formed due to exposure to corrosive environments either topside, Figure 4, or in humid internal environments, Figure 5.

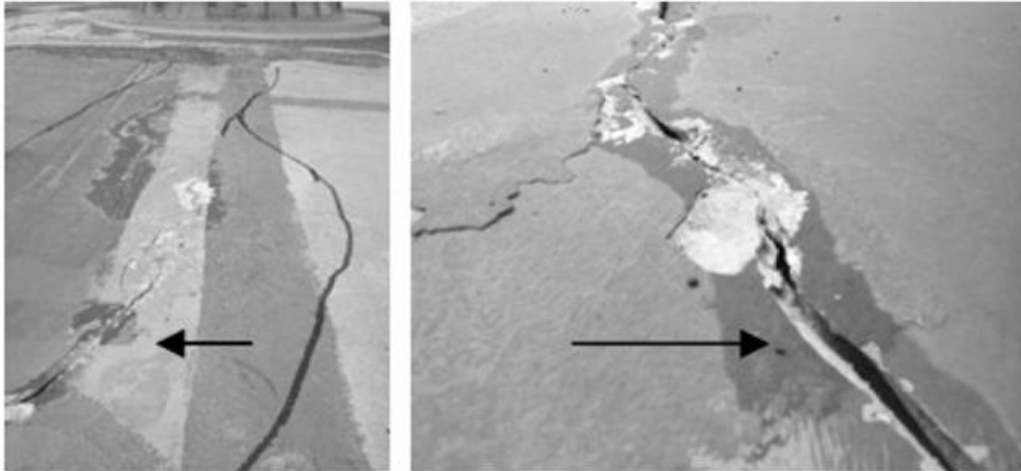


Figure 4. AA5456-H116 Direct weather exposed deck-plate displaying stress corrosion cracking. (From Schwarting et al. [5])



Figure 5. AA5456-H116 Interior structure exposed to conductive heat and corrosive humid environment. (From Schwarting et al. [5])

Emergent repairs have been increasing in numbers and severity since the initial discovery of SCC on the first cruiser. The Department of Defense spends approximately \$22 billion dollars annually on corrosion, with 23.2% of this spending used to repair Navy ships and so far, the permanence of many of these repairs is unknown [10]. The cost for civilian corrosion infrastructure is similar in cost and magnitude. Due to the evidence that two types of corrosion are occurring on surface vessels, SCC and corrosion

fatigue, and that corrosion fatigue is potentially a synergistic mechanism between fatigue and SCC, the study of the both types of corrosion cracking is necessary to effectively develop corrective and preventative solutions.

B. INTRODUCTION

There are several 5xxx series aluminums currently in use on marine vessels (e.g. 5456, 5083, 5086, 5454, etc.) that are summarized in Table 1. While the rudimentary properties of these aluminums are similar, their behaviors can be very different, especially under complex loadings in corrosive environments. More is known about the corrosive behavior of prevalent materials such as AA5083, but stress corrosion cracking behavior of AA5456 has yet to be fully characterized.

	Composition									Strength (MPa)			Modulus of Elasticity (MPa x 10 ³)
	Mg	Mn	Fe	Si	Cr	Ti	Zn	Cu	Al	Ultimate	Yield	Hardness	
5456	5.1	0.64	0.18	0.11	0.09	0.02	0.02	0.01	remainder	350	255	90	71
5083	4.7	0.9	0.2	0.1	0.08	0.01	0.03	0.03	remainder	315	230	85	71
5086	4.0	0.45	0.5	0.4	0.15	0.15	0.25	0.1	remainder	290	205	78	71
5454	2.7	0.08	-	-	0.12	-	-	-	remainder	260	180	70	70

Table 1. Comparison of composition and mechanical properties of several 5xxx series aluminums. (From Kaufman, [11])

Research by Holtz et al. determined the ΔK_{th} of sensitized AA5083 in salt water [12], while work at Alcoa by Bovard et al. has produced stress corrosion crack growth rate and crack velocity data for sensitized AA5083 [13]. Brosi et al. determined the ΔK_{th} of sensitized AA5456 in air [14] and Menzemer et al. determined ΔK_{th} of as received AA5456 in pure water vapor [15]. These values are summarized in Table 2. With SCC and corrosion fatigue data on sensitized AA5083 in salt water available, data on how the level of sensitization affects the ΔK_{th} of AA5456 in salt water and stress corrosion crack growth rate and crack velocity of sensitized AA5456 can be used to compare the effect of a higher Mg content in AA5456 compared to AA5083. Without the fundamental parameters such as plane strain fracture toughness (K_{IC}), the resistance to crack growth in a corrosive marine environment, or the threshold stress intensity factor (K_{th}), defined as the lowest stress intensity when crack growth does not occur, effective ways to predict material failure and mitigate SCC in AA5456 cannot be identified.

	AA5083	AA5456
K_{IC} (MPa√m)		
	33 (S-L)	23±5 (S-T)
K_{ISCC} In Splash/Spray (MPa√m)		
As-Received	9.3	
Mass Loss 21.7 mg/cm ²	8.23	
Mass Loss 32.5 mg/cm ²	4.94	
ΔK_{th} In Vacuum (R = 0.1) (MPa√m)		
As-Received	1.2	
Sensitized at 175°C for 240 hours	1.2	
ΔK_{th} In Air (R = 0.1) (MPa√m)		
As-Received	1.09	2.8
Sensitized at 175°C for 10 hours		2.7
Sensitized at 175°C for 100 hours		2.1
Sensitized at 175°C for 240 hours	1.09	
ΔK_{th} In Pure Water Vapor (R = 0.1) (MPa√m)		
As-Received		8
ΔK_{th} In Salt Water (R = 0.1) (MPa√m)		
As-Received	1.08	
Sensitized at 175°C for 240 hours	1.08	

Table 2. Comparison of K_{ISCC} and ΔK_{th} values for AA5456 and AA5083 from literature. (From Holtz et al. [12]; Bovard et al. [13]; Brosi et al. [14]; and Menzemer et al. [15]; Crane [16])

1. Stress Corrosion Cracking

The undesired effect of sensitization is the increased susceptibility to corrosion and, for structures in operation, stress corrosion cracking. For SCC to take place, three conditions are required: a susceptible material, a corrosive environment, and a tensile stress; their mutual dependence is shown in Figure 6. If any of these three conditions are removed, SCC will not occur.

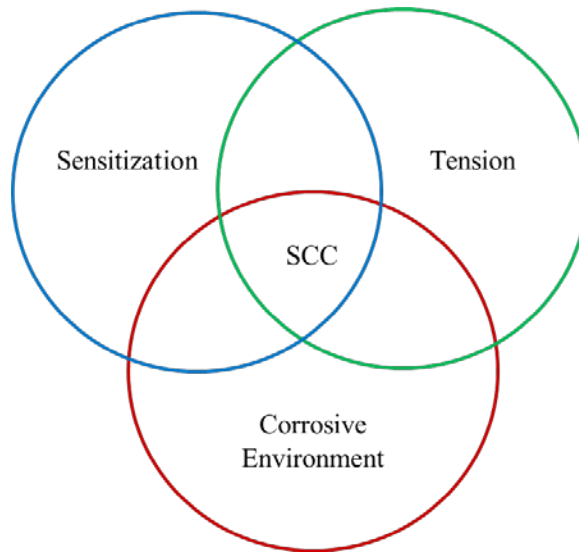


Figure 6. Venn Diagram showing the mutual importance of Sensitization, Tensile Stress and Corrosive Environment on SCC.

AA5456 is considered a susceptible material when it is sensitized to the extent where the β precipitate phase approaches continuity along grain boundaries. The β phase is more anodic than the surrounding material matrix and therefore is electrochemically more active, increasing its susceptibility to corrosion [17]. The marine environment in which ships exist is extremely corrosive, and studies have found that vapor phase s corrosive environments and environments where the material alternates between wet and dry, splash and salt spray environments, are more aggressive then full immersion [13]. The final contribution to SCC is the presence of a tensile stress. Stresses can either be applied, such as ship movement in the form of hogging and sagging, machinery vibration, or payload; or residual, caused by welds, bolts, or rivets.

A material's degree of susceptibility to intergranular corrosion is dependent on several variables including sensitization temperature, stress orientation, and type of corrosive environment. The nitric acid mass loss test, ASTM G67 [9], is the standard test method in the Department of Defense (DoD) for determining the susceptibility to intergranular corrosion of 5xxx series aluminum alloys. This test provides a quantitative measure of the degree of sensitization by comparing the change in weight of samples both before and after exposure to nitric acid. The nitric acid preferentially dissolves the beta phase; thus the mass loss represents the amount of beta phase in the alloy. Under

this test, a sample with a measured mass loss greater than 25 mg/cm² is considered to be susceptible to intergranular forms of corrosion [9]. While the presence of a continuous intergranular network of β -phase would result in relatively large mass losses due to grain boundary fall out, nitric acid attacks intragranular β -phase as well. A more comprehensive determination of sensitization requires metallography to examine the relative ratios of intragranular versus intergranular β -phase.

The degree of sensitization of 5xxx series aluminums is temperature and time dependent. Oguocha et al. found that the critical temperature at which AA5083-H116 is most susceptible to IGC, i.e. the temperature where the most magnesium atoms come out of solid solution and migrate to grain boundaries, lies between 150°C and 200°C. Specifically, Figure 7 shows a sensitization temperature of 175°C produced the most mass loss per unit area, even more so than exposure to higher temperatures for the same amount of time. Holtz et al. found in Figure 8 that as sensitization time increases at a temperature of 175°C, the β -phase in AA5083 becomes increasingly more continuous, ultimately resulting in more grain boundary fall out compared to other sensitization times. This finding is similar to the work by Goswami et al. who also found that grain boundary continuity of the β -phase is achieved in AA5083 after a sensitization time of 240 hours at 175°C [18]. The reduction in the hardness and strength of the specimens sensitized at elevated temperatures for a long time is due partly to recrystallization and partly to a reduction in the concentration of magnesium atoms in solid solution [14, 19].

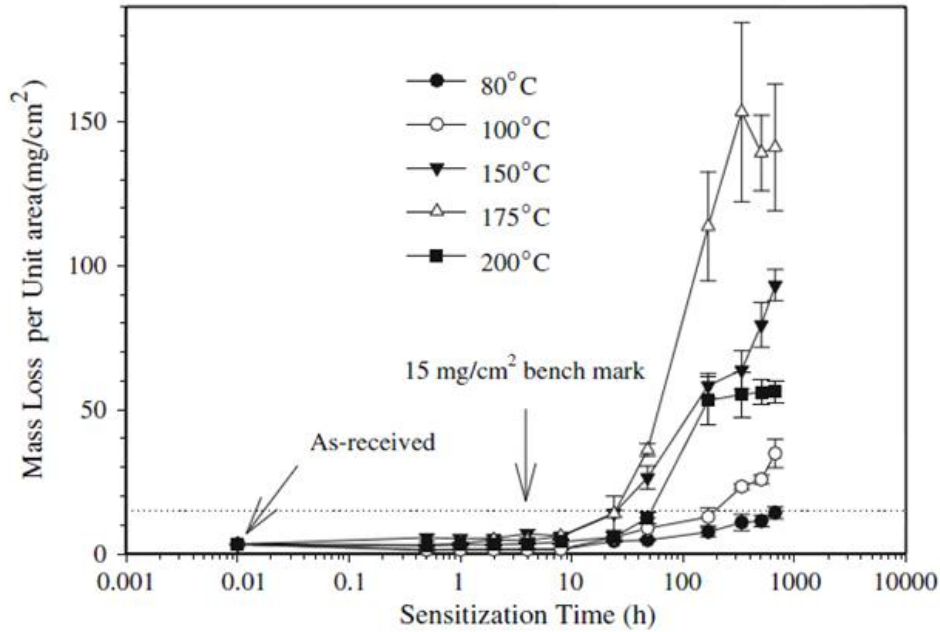


Figure 7. Effect of sensitization temperature and time on IGC susceptibility of AA5083-H116. (From Oguocha et al. [19])

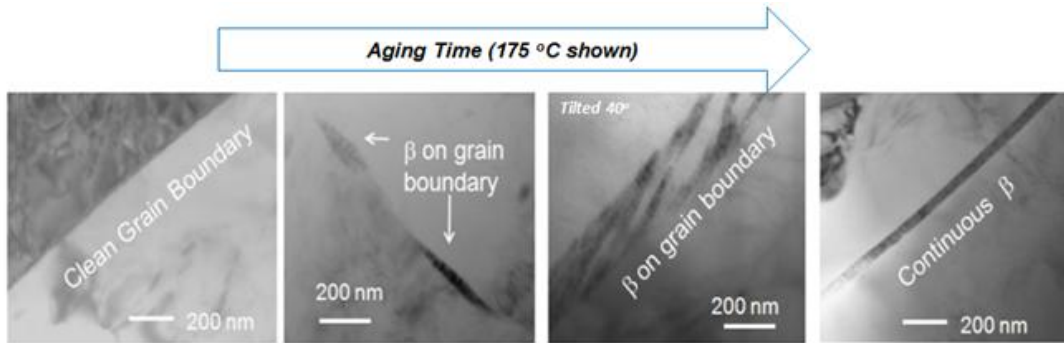


Figure 8. Microstructure Evolution of AA5083 at 175°C. (From Holtz et al. [12])

The crack growth rate of 5xxx series aluminum is sensitive to details of the type and distribution of β -phase in the material. Bovard attributes the dramatic increase in crack growth rates for sensitization levels of 32 - 44 mg/cm^2 (Figure 9) to the possibility of a critical mass loss, grain boundary discontinuities, or the existence of a critical sensitization temperature during thermal exposure [20]. The temperature that AA5456 is exposed to is equally as influential as the length of time that the aluminum is exposed. At temperatures below 260°C, the precipitate phase that forms first is not the equilibrium β -phase but a metastable phase (β') and depending on the thermal exposure temperature

and time, varying percentages of both phases can form. Bovard postulates that it is possible that if the precipitate formed at 175°C is different than the precipitate formed at lower sensitization temperatures then the increase in crack velocity could also be related to a difference in the structure or composition of the grain boundary precipitate [20]. Crack velocities were also found to increase at K_I values over 7.686 MPa \sqrt{m} (Figure 10) in AA5083 double cantilever beam samples exhibiting mass losses of 44 mg/cm² that were subjected to a corrosive 3.5% NaCl solution via intermittent exposure.

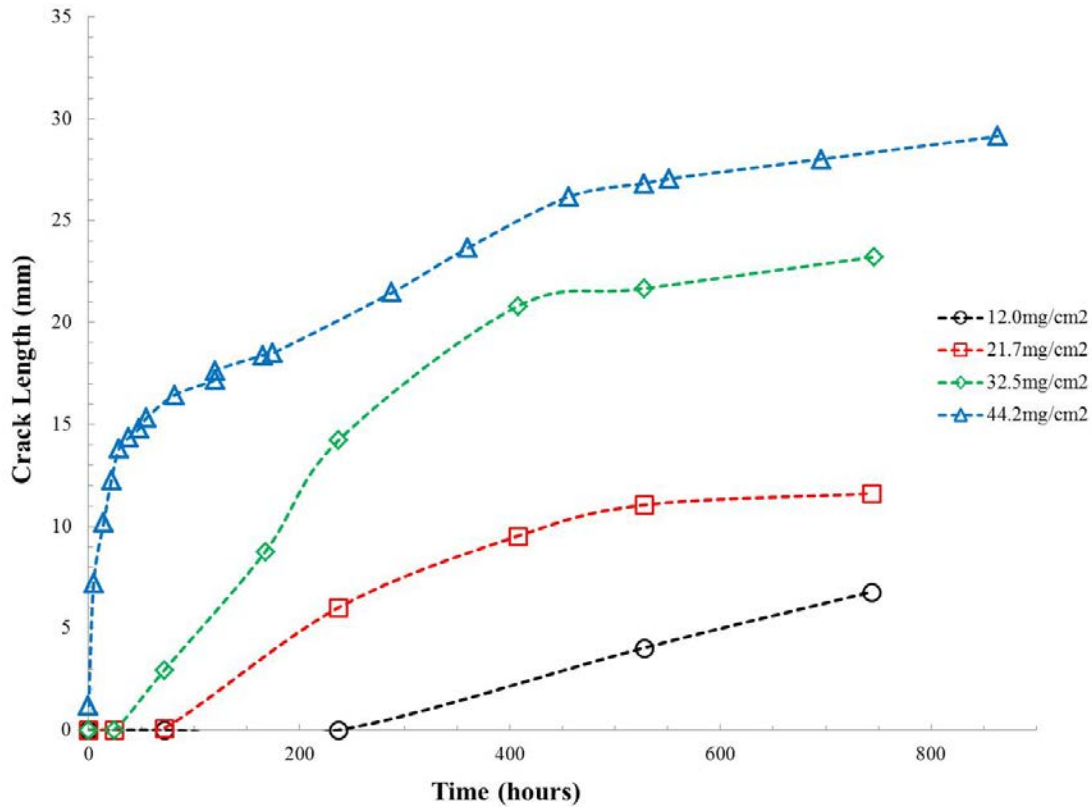


Figure 9. Increases in Mass Loss in ASTM G67 Correspond to Increases in S-L DCB Crack Growth Rates. Data converted to metric units. (From Bovard, [13])

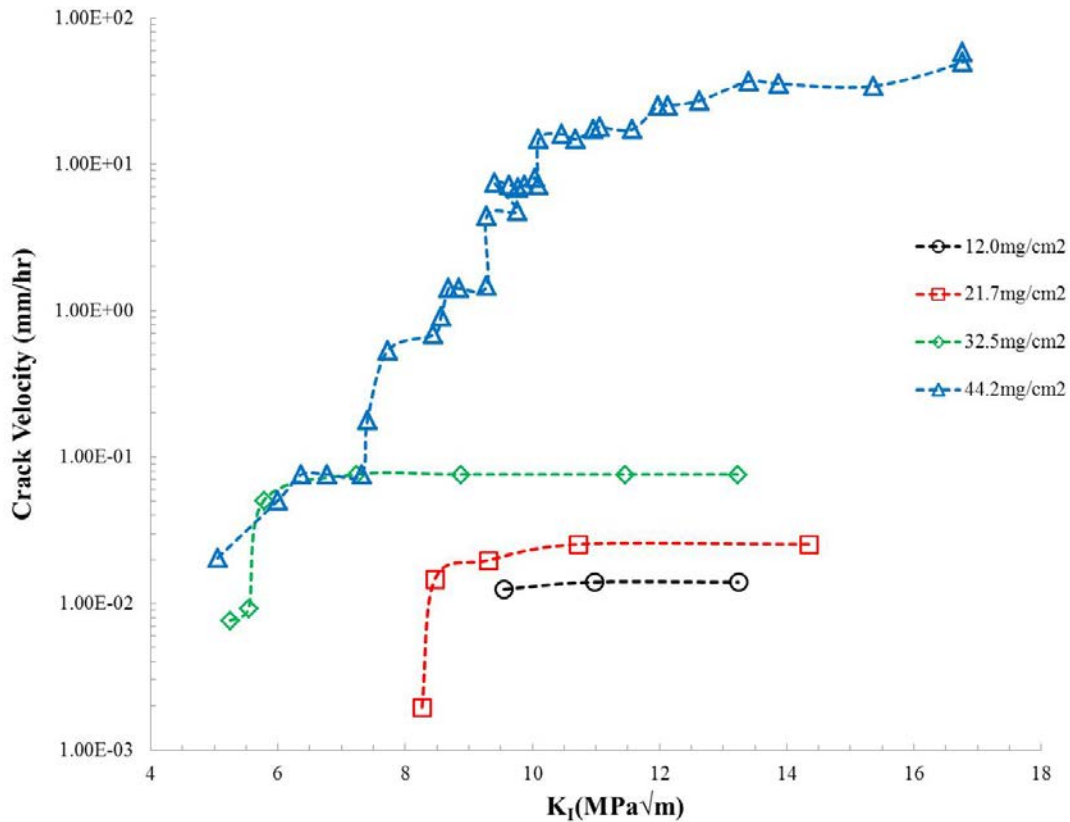


Figure 10. Increases in Mass Loss in ASTM G67 Correspond to Increases in S-L DCB Crack Growth Rates at Various Stress Intensity Factors. Data converted to metric units. (From Bovard, [13])

Temperature and time are not the only factors when it comes to sensitization and its effect on the mechanical properties of aluminum. The microstructure of the material plays a strong role in the sensitization and subsequent fracture behavior of the 5xxx series aluminums mainly due to the cold working (rolling) during the fabrication process. Rolled aluminum plate is an anisotropic material resulting in the fracture strength having a directional dependence. Brosi et al. found the presence of longitudinal splitting and delamination in sensitized AA5456 tested in air in Figure 11. The delamination is attributed to applied transverse stresses of sufficient magnitude to cause fracture along grain boundary regions that are weakened by the evolution of grain boundary segregation and precipitation associated with sensitization [14]. Fracture in this orientation can also occur through exfoliation corrosion where surface layer grains are lifted up and flaked off as corrosion proceeds intergranularly.

A strong connection between sensitization, delamination, and the threshold stress of AA5456 also exists. At ΔK_{th} , cyclic stress levels are insufficient to delaminate the material regardless of degree of sensitization; however, the increasing severity of delamination with increasing ΔK indicates that a critical regime for delamination exists with regard to exposure time and temperature [14]. DCB testing on AA5083 has also demonstrated that for mass losses between 32 to 44 mg/cm², AA5083 samples fail rapidly when tested in the short transverse (ST) orientation but do not fail in the long transverse (LT) orientation even after extended exposure to a 3.5% NaCl solution. The rapid failures at the low ST stress levels indicate that the SCC threshold stress (K_{ISCC}) in the ST orientation is very low and that there is a strong dependence of SCC susceptibility on loading orientation [20].

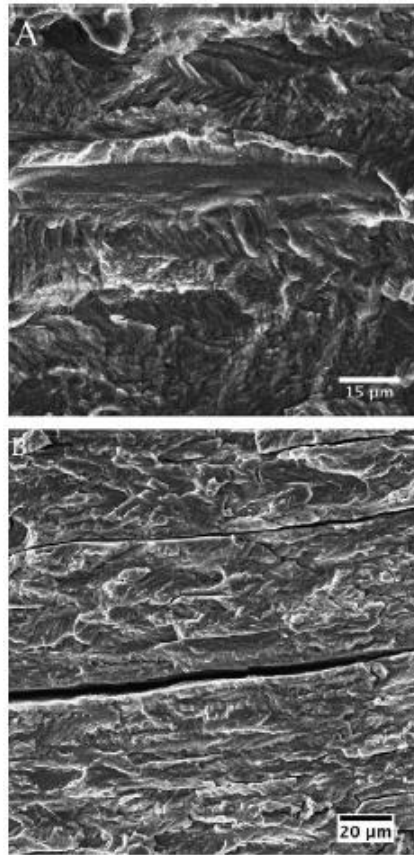


Figure 11. Comparison of SEM fractograph of (A) as-received 5456-H116 and (B) 5456-H116 exposed to 175°C for 100 h. There was significant delamination in (B), while none was exhibited in (A). (From Brosi et al. [14])

2. Stress Corrosion Crack Propagation

SCC promulgates through three stages: (1) initiation or incubation; (2) propagation; and (3) failure or arrest. The initiation of SCC can occur at a critically-sized surface flaw in the material that when combined with a tensile stress results in crack formation. Common surface flaws found on ships are weld joints, surface scratches, and sharp fillets. In addition, corrosion processes such as pitting and exfoliation, can naturally cause damage and nucleate cracks. The natural progress of IGSCC starting on the surface of AA5083 and proceeding in three directions is documented in Figure 12.

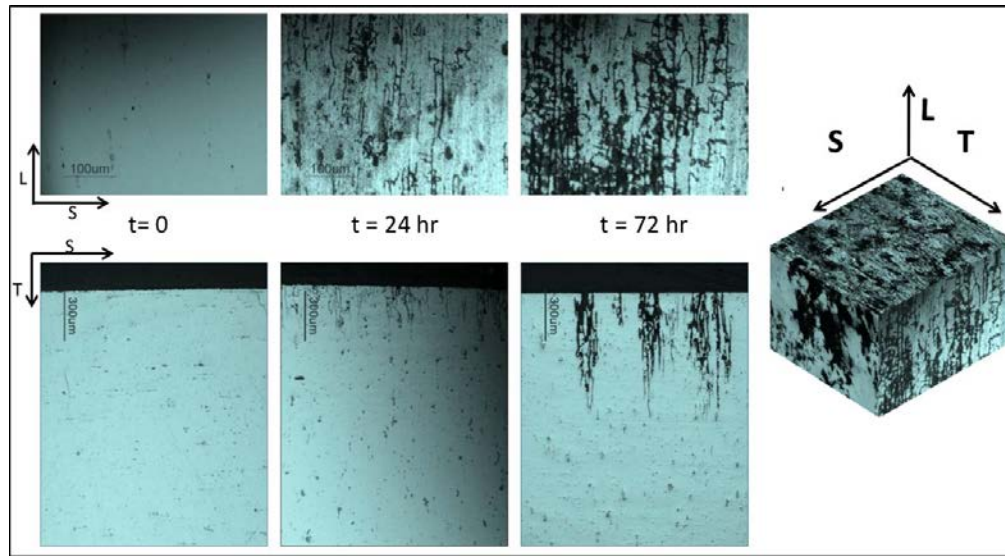


Figure 12. Intergranular corrosion starting on the surface of AA5083. (From Scully et al.[21])

After a crack is initiated, the crack will only grow through SCC when the stress intensity exceeds that required for SCC in Equation (1). That is, the applied stress intensity factor, K_I is equal to or larger than the SCC resistance parameter (K_{ISCC}), a material and environment dependent property [22].

$$K_I \geq K_{ISCC} \quad (1)$$

K_{ISCC} can be obtained through fracture mechanics testing of a given material in the environment of interest. The value for K_I as a function of crack length is also

required for this model and can be calculated through Equation (2) where β is a shape factor corresponding to the crack and the structural component and σ is the tensile stress.

$$K_I(a, \sigma) = \beta \sigma \sqrt{\pi a} \quad (2)$$

Combining the fracture criterion for SCC and the stress intensity expression results in the derivation of the critical flaw size required for SCC initiation and propagation in Equation (3).

$$a_{initiation} \geq \frac{1}{\pi} \left(\frac{K_{ISCC}}{(0.80 * \sigma_{yield}) \beta(a/W)} \right)^2 \quad (3)$$

The crack length, a , grows as a function of time and therefore the prediction of the final fracture requires the ability to predict the crack growth rate for a specific material in a specific environment. The critical flaw size, or minimum flaw size resulting in final fracture, under elastic loading, is determined from the threshold stress intensity factor (K_{ISCC}), a material dependent property. Using AA5083-H116 as an example, the yield strength of 215 MPa, and K_{ISCC} of 9.3 MPa \sqrt{m} (Figure 10 [13]) is used in the above equation along with a sample thickness of 2 mm to determine the critical flaw for SCC initiation to be 346 μm .

3. Stress Corrosion Cracking Mechanisms

While the preceding discussion describes the mechanics for crack nucleation and can be extended to crack propagation, it does not describe the interaction between electrochemistry and microstructure that controls the rate of crack propagation. Once a critical flaw is reached, the initial mechanism of crack propagation in 5xxx series aluminum alloys is regarded to be local and preferential anodic dissolution of the β -phase. When salt water is the corrosive environment, aluminum (hydroxy) chlorides are the hydroxides formed due to the adsorption of Cl^- on the hydroxide surface layer as well as anion exchanges between OH^- and Cl^- . The eventual breakdown of the passive Al_2O_3 oxide layer and the dissolution of the aluminum substrate are enhanced in saltwater due to the high concentration of chloride ions in saltwater [23]. Additionally, the Al_3Mg_2 β -phase has been found to have an open-circuit potential of -1.01 V, which when compared

to the open-circuit potential of Al which is -0.823 V, results in the conclusion that this grain boundary phase is anodic to the grain matrix and active for corrosion, compared in Table 1. This anodic nature, supports the theory that selective dissolution of the β -phase grain boundaries is a key driving force for IGSCC in these materials [17]. Although there is wide agreement that anodic dissolution of the beta phase drives IGSCC in marine grade aluminums, there is substantial disagreement about the exact mechanism for IGSCC crack propagation.

Stoichiometry	Phase	Corrosion potential (mV _{SCE})			Note
		0.01 M	0.1 M	0.6 M	
Al ₃ Fe	β	-493	-539	-566	
Al ₂ Cu	θ	-592	-665	-695	
Al ₃ Zr	β	-752	-776	-801	
Al ₆ Mn	-	-839	-779	-913	
Al ₃ Ti	β	-620	-603	-799	
Al ₃₂ Zn ₄₉	T'	-1009	-1004	-1063	
Mg ₂ Al ₃	β	-1124	-1013	-1162	
MgZn ₂	M, η	-1001	-1029	-1095	
Mg ₂ Si	β	-1355	-1538	-1536	
Al ₇ Cu ₂ Fe	-	-549	-551	-654	
Mg(AlCu)	-	-898	-943	-936	
Al ₂ CuMg	S	-956	-883	-1061	
Al ₂₀ Cu ₂ Mn ₃	-	-550	-565	-617	
Al ₁₂ Mn ₃ Si	-	-890	-810	-858	
Al (99.9999)	-	-679	-823	-849	A
Cu (99.9)	-	-177	-232	-220	A
Si (99.9995)	α	-450	-441	-452	A
Mg (99.9)	-	-1601	-1586	-1688	A
Mn (99.9)	-	-1315	-1323	-1318	A
Cr (99.0)	-	-495	-506	-571	A
Zn (99.99)	-	-985	-1000	-1028	A
Al-2%Cu	α	-813	-672	-744	B
Al-4%Cu	α	-750	-602	-642	B
7X75 Matrix	-	-699	-799	-812	M
AA 7075-T651	-	-816	-965	-1180	X

Table 3. Corrosion potentials for intermetallic compounds common in aluminum alloys. (From Birbilis, [24])

There are several theories that are used in the literature to describe the mechanism of environmental crack propagation in 5xxx aluminum alloys, with three reviewed here: (1) IGSCC propagation via the classic film rupture model; (2) environmental crack propagation by mechanism involving hydrogen embrittlement, and (3) IGSCC propagation via corrosion tunneling. When modeling IGSCC in 5xxx aluminum, one must consider several specific material characteristics of this alloy family: passive film

stability and repassivation kinetics; anodic dissolution kinetics at the sensitized grain boundary, and the ductility and yield strength. In all three of the theories explored here, the anodic dissolution of the β -phase is of key importance. For the film rupture model and model involving hydrogen embrittlement the passivation behavior of aluminum is central. For the model that relies on corrosion tunneling, the ductility and low yield strength of 5xxx aluminum are dominant factors. However, all three models depend heavily upon the details of the electrochemistry at the crack tip and how this crack tip interacts with the microstructure.

The electrochemistry behind IGSCC in sensitized 5xxx aluminum can be most easily described by the anodic oxidation and dissolution of the β -phase precipitates at the sensitized grain boundary, and the coupled cathodic reduction reactions that much accompany the anodic process with the crack. The anodic reaction for the anodic oxidation of aluminum to form trivalent aluminum cations is described by Equation (4).



In cases involving the anodic dissolution of the β -phase precipitates, in addition to the anodic oxidation of aluminum, the anodic oxidation of magnesium to form divalent cations is also important as shown in Equation (5).



The electrons provided by these oxidation reactions are consumed by several possible reduction reactions that must occur in parallel, including the reduction of oxygen that is dissolved in the environment (cathodic reaction) in Equation (6).



In the cases of IGSCC, the reduction of oxygen may occur primarily at the mouth of the crack, where abundant oxygen is present. In addition, protons in the salt water can be reduced to atomic or molecular hydrogen in Equation (7).



The relative rates of formation of hydroxyl anions and consumption of hydrogen ions (protons) in the aqueous electrolyte in contact with the crack is controlled primarily by the solubility of oxygen at the outer surface, or by the acidity of the electrolyte.

Stress corrosion cracks, like crevices and pits are occluded geometries, and as such can support differential aeration, with substantial oxygen reduction at the mouth of the crack, and anaerobic conditions inside the crack. Under the anaerobic conditions within the crack, the hydrolysis of the aluminum and magnesium produced by the reactions shown in Equations (6–7) can lead to acidification within the crack, and as a consequence, passive film destabilization. These hydrolysis reactions are shown below as Equations (8–9). SCC is known to occur in regions of the Pourbaix diagram (combinations of potential and pH) where the passive film exists, but has marginal stability. An environment that allows for rapid mass transport, e.g. a salt water vapor, will provide sufficient oxygen for the formation of hydroxyl ions to dominate the electrochemistry driving IGSCC. Benedictus-deVries et al. compare the mechanism of stress corrosion crack propagation to that of localized crevice corrosion. During SCC, the narrow crack entrance prevents the continual refreshment of the corrosive environment therefore creating an environment inside the crack that is oxygen deprived resulting in a low pH. The cathodic reaction in Equation (6) will first take place near the dissolution of the aluminum, which is inside the crack. Due to the fact that the crack is oxygen deprived, the reduction of oxygen will then take place on the outer surface of the metal (neutral to alkaline pH). This potential drop between the outer surface of the metal and the crack tip will lead to an electron transport through the aluminum [23]

The type of corrosive environment has been found to affect the severity of IGSCC in 5xxx series aluminums. There is a preponderance of experimental data showing that fatigue crack growth rates are a function of the rate of transport of water vapor from the environment to the tip of the advancing crack and the surface reaction kinetics that occur at the crack tip [13, 15, 25, 26]. Water vapor, both pure and containing salt, is transported more quickly to the crack front compared to full immersion of the cracked material. A gaseous environment increases the rate of supply of the aggressive environment to the crack front. Additionally, oxygen is more soluble in vapor than liquid

that is, water vapor contains more oxygen than pure liquid water resulting in a higher concentration of oxygen at the crack front in gaseous environments. Table 4 shows that the combination of liquid and gaseous exposure of sensitized U-bend specimens resulted in the fastest time to failure compared to full immersion and total gas.

Test Environment	Orientation	F/N	Time to Failure (weeks)
Seacoast Atmosphere	LT	5/5	3,3,3,3,3
Splash/Spray	LT	5/5	1,1,1,1,1
Full Immersion	LT	3/5	2,2,4,R,R
Tidal	LT	5/5	1,1,1,1,1
Notes: F/N = Failures/Number of specimens exposed; R = Removed from test unfailed at 6 months exposure			

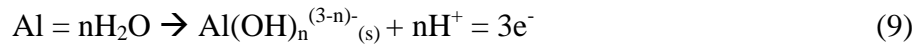
U-bend specimens made with material intentionally sensitized to a mass loss of 47 mg/cm²

Table 4. Time to Failure for various types of environmental exposure.
(From Bovard, [13])

The passivation and repassivation kinetics are complex in this alloy family, but are of central importance for describing IGSCC. The hydroxides formed by aluminum occur due to the hydration of the passive aluminum oxide (Al₂O₃), which forms as a protective layer on the surface of the metal between the aluminum and the corrosive environment. The reactions associated with the creation of hydroxides are simplified in Equation (8) due to the fact that hydration occurs in many stages and therefore the resulting compositions of the Al₂O₃ can vary [23].



The formation of hydroxides is now driven by the anodic reaction in Equation (9).



The Pourbaix diagram show in Figure 13 illustrates the process explained above where more negative potentials provide corrosion immunity at all pH levels, and corrosion occurs at pH levels on either side of the range 4 to 8 at potentials more positive than -1.5 E(V).

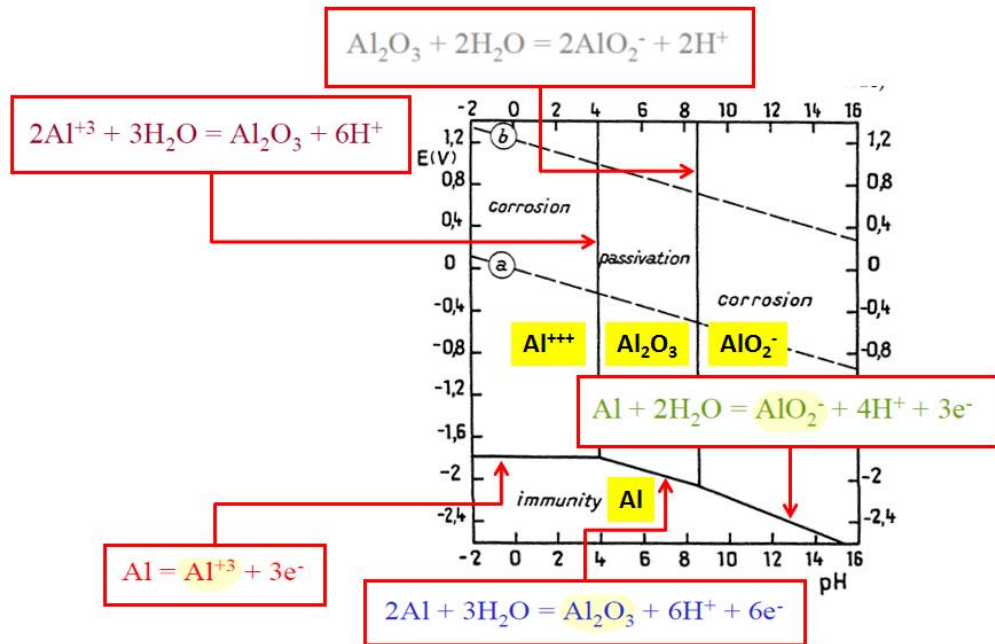


Figure 13. Pourbaix diagram for aluminum showing corrosion, passivation, and immunity regions as a function of pH and potential. Chemical reactions for separation lines are indicated. (From Pourbaix, [27])

The first potential mechanism for crack propagation in 5xxx series aluminums is the film rupture model, illustrated in Figure 14. In this model, SCC is related to and is accelerated by, increases in pH and potential due to the chemistry of the oxide phase present at the crack front. The film-rupture model has been applied to SCC in stainless steel, low-alloy steel, and nickel-based alloys [28].

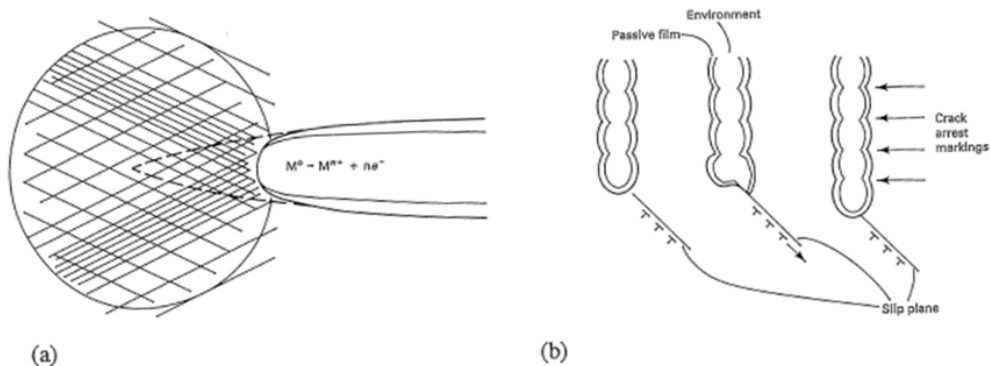


Figure 14. Schematic representation of crack propagation by the film-rupture model. (a) Crack tip stays bare as a result of continuous deformation. (b) Crack tip passivates and is ruptured repeatedly. (From Farmer, [29])

The model is represented by Equation (10) where V_t is the crack propagation rate (cm s^{-1}) and $\dot{\epsilon}_{ct}$ is the crack-tip strain rate (s^{-1}). The crack tip strain rate is proportional to the stress intensity. The constants A and n are dependent on the material and crack tip environment and are determined from the measured rate of repassivation.

$$V_t = A(\dot{\epsilon}_{ct})^n \quad (10)$$

These repassivation parameters are critical because the film rupture model depends upon repeated repassivation to keep the crack tip sharp and thus propagate the crack into the material.

Hydrogen embrittlement provides an alternative theory for crack propagation and is illustrated in Figure 15. Menzemer et al. describe hydrogen embrittlement as the governing mechanism for accelerated crack growth in AA5456. Jones et al. further described the process of crack growth through hydrogen embrittlement for AA5083 in several steps [25]:

- Preferential corrosion of the β -phase
- β -phase corrosion results in the conversion of the β -phase into Al_2O_3
- Hydrogen is generated during the corrosion of the β -phase
- This hydrogen is then absorbed and diffused ahead of the crack
- The subsequent crack growth occurs simultaneously with hydrogen uptake

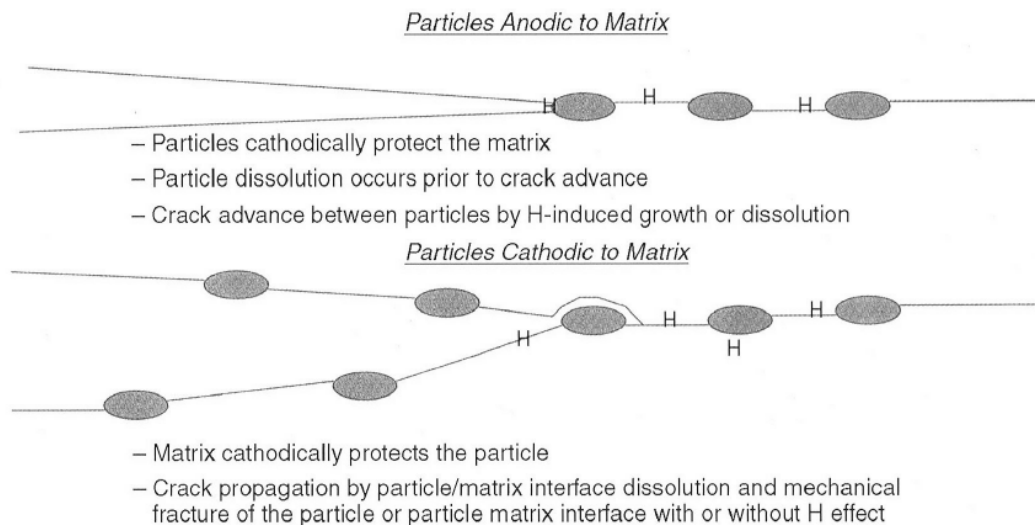


Figure 15. Schematic showing possible crack-tip/particle interactions for electrochemically active particles. (From Jones, [26])

Jones et al further explained that when the β -phase is not continuous, the crack advances between particles occurs through hydrogen-induced processes. Searles et al. also discussed the hypothesis of hydrogen absorption resulting in crack growth in 5xxx series aluminums. They point out that pure Al and other Mg-free alloys exhibit a low hydrogen permeability compared to alloys with Mg segregation. The fact that unsensitized, Al-Mg alloys show immunity to SCC under hydrogen permeation; while sensitized Al-Mg alloys with grain boundary precipitation exhibit SCC under these conditions, strongly suggests that hydrogen embrittlement play a central role for IGSCC in sensitized 5xxx alloys [17].

The final possible mechanism for SCC propagation in 5xxx series aluminums is the corrosion tunneling model, illustrated in Figure 16. In this model, the assumption is that fine arrays of small corrosion tunnels form from the anodic dissolution of the beta phase. These corrosion tunnels grow until the stress in the remaining ligaments causes ductile deformation and finally fracture [30]. The hallmark of this model is a grooved fracture surface showing evidence of microvoid coalescence on the peaks of the grooves. The addition of a tensile stress on samples undergoing SCC may result in the flattening of these peaks and fracture surfaces appear to be flat slots as opposed to tunnels. It is possible that the preferential dissolution of the β -phase in marine grade aluminum results

in crack propagation along grain boundaries through the corrosion tunnel model, where the β -phase acts as an initiation site and the tunnels expand thus propagating the crack. The low yield strength and ductility of 5xxx alloys makes this mechanism particularly interesting.

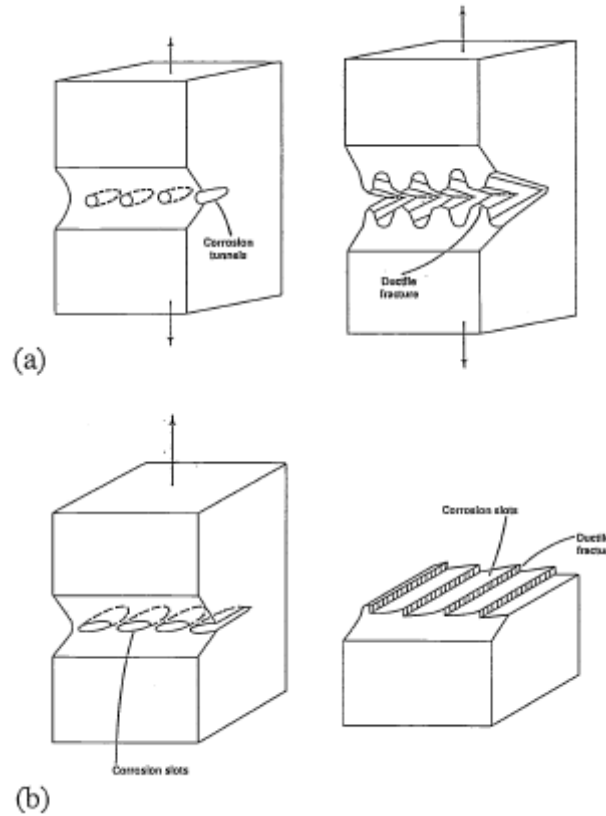


Figure 16. Illustration of corrosion tunnel model. (a) Schematic of tunnel model showing the initiation of a crack by the formation of corrosion tunnels at slip steps and ductile deformation and fracture of the remaining ligaments. (b) Schematic diagram of the tunnel mechanism of SCC and flat slot formation. (From Jones, [30])

4. Corrosion Fatigue

Corrosion fatigue is the acceleration of the fatigue failure of materials by exposure to a reactive environment. As a failure mode, fatigue crack propagation is the predominant mode of failure in metals and accounts for 90% of failures in all material types [31]. This statistic along with the cyclic nature of ship movement (hogging and sagging) results in the determination that the driving force for most crack propagation on

ships is fatigue loading. The classifying parameter for fatigue failure is the fatigue endurance limit, defined as the amount of stress that can be repeatedly applied to a metal, generally beyond 10 million cycles for high cycle fatigue, below which no cracking will occur. Failure due to fatigue occurs at stress levels well below the ultimate, or yield strength of the material and for aluminum alloys a clear fatigue endurance limit, or threshold, often does not exist.

Stress-cycle or SN charts (plot of $\Delta\sigma$ vs. N) are used to show the influence of fatigue loading parameters on the fatigue life of a material component. As $\Delta\sigma$ becomes larger, the number of cycles to failure (N) becomes much less. Figure 17 shows the overlay of two S-N charts, one for 1045 Steel, and another for 2014-T6 Al. As shown, aluminum that exhibits a continuous decrease in required stress for failure as the number of cycles increases, with no clear stress value under which the material will not fail. Problems with fatigue failure can be exacerbated when combined with the corrosive marine environment, a failure mode classified as corrosion fatigue.

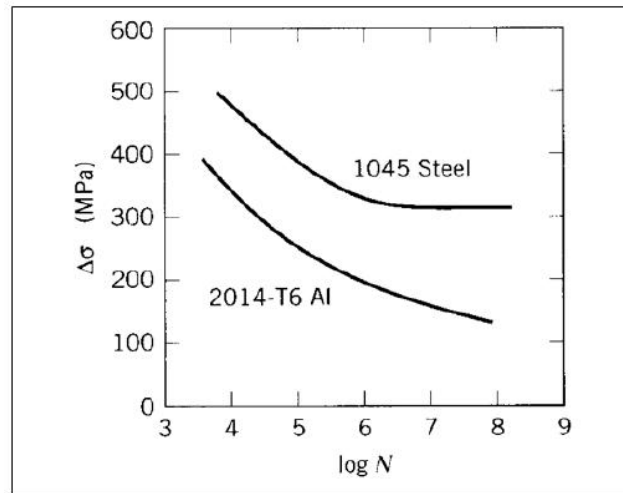


Figure 17. Stress amplitude (S) versus logarithm of the number of cycles to fatigue failure (N) comparison between steel that does have a fatigue limit and aluminum that does not have a fatigue limit. (From Schwarting et al. [5])

All forms of fatigue failure are described by details of the stress profile on the component over time. If a ship is modeled as a beam, the cyclic motion of a ship in water defined earlier as hogging and sagging can be represented as the maximum stress (σ_{\max})

and minimum stress (σ_{\min}) placed on the ship, respectively [32]. From these values the mean stress (σ_m) can be calculated through Equation (11), the stress ratio (R) can be calculated through Equation (12) and the stress amplitude (σ_a) can be calculated through Equation (13).

$$\sigma_m = \frac{(\sigma_{\max} + \sigma_{\min})}{2} \quad (11)$$

$$R = \frac{\sigma_{\min}}{\sigma_{\max}} \quad (12)$$

$$\sigma_a = \frac{(\sigma_{\max} - \sigma_{\min})}{2} = \frac{\sigma_r}{2} \quad (13)$$

In the limit of $R=1$, the amplitude stress goes to zero, thus change the loading from cyclic to monotonic loading at the value of the mean stress.

For the purposes of this diagram, σ_{\max} is unity as is the crack length. The geometrical parameter, Y, is assigned as the square root of π only as an example.

In addition, increases in mean stress will lower the entire S-N curve (Figure 17). Mean stress and the stress amplitude can be related through the ultimate strength (σ_{ult}) and the fatigue limit (σ_{fat}) of the material as is commonly done in the Goodman relationship in Equation (14) and the Gerber relationship in Equation(15).

$$\sigma_a = \sigma_{\text{fat}} \left[1 - \frac{\sigma_m}{\sigma_{\text{ut}}} \right] \quad (14)$$

$$\sigma_a = \sigma_{\text{fat}} \left[\frac{\sigma_m}{\sigma_{\text{ut}}} \right]^2 = 1 \quad (15)$$

As the mean stress is decreased, the relationship between σ_a and N_f shifts toward the upper right hand corner of the stress-cycle plot, thus predicting a longer fatigue life for a given applied stress. The residual stresses associated with processes such as shot-peening are negative or compressive, thus reducing the mean stress and theoretically increasing the fatigue life of a material that has experienced cyclic loading.

Fatigue crack propagation is better represented by examining the crack growth rate as a function of applied stress intensity factor. This relationship can be shown using a da/dN versus ΔK plot, where a is the crack length, N is the number of cycles, and ΔK is the range of the stress intensity factor in a loading cycle (Figure 18).

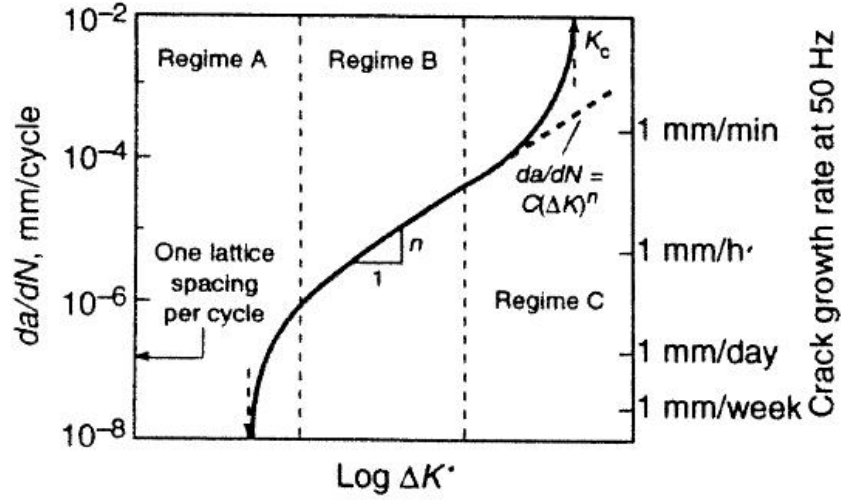


Figure 18. Schematic illustration of the different regimes of stable fatigue crack propagation. (From McEvily, [33])

The fatigue crack threshold (ΔK_{th}) and fracture toughness (K_{IC}) are shown as the bounds on this plot, the former showing the onset of fatigue crack growth and the latter showing the transition to final, fast fracture. In between, stable fatigue crack growth is observed and can be described by the Paris Law approach in Equation (16), which is characterized by the regression exponent, n .

$$\frac{da}{dN} = C(\Delta K^n) \quad (16)$$

In this equation, da/dN is the crack growth rate, C is the regression coefficient, and ΔK is the stress intensity range. Equation (16) can be rearranged and integrated to obtain the high-cycle fatigue life for a series of constant amplitude stress range values in Equation (17).

$$N = \int \frac{da}{C(\Delta \sigma \beta \sqrt{\pi a})^n} \quad (17)$$

The stress range, $\Delta\sigma$ is described above in Equations (11-13) and da is the change in crack length. The plots in Figure 19 and Figure 20 show that there is a difference between the number of cycles to failure, N , between tests conducted with $R = 0.1$ and test conducted with $R = 0.85$. As the R value gets closer to one the mean load increases resulting ΔK_{th} decreasing as R increases. The ability to predict the fatigue life of 5xxx series aluminums in corrosive conditions is a valuable tool in preventing unstable crack propagation resulting in permanent and expensive damage to ships.

A corrosive environment adds complexity to analyzing fatigue life data by increasing crack growth rates while also increasing the crack tip closure effect, in turn decreasing ΔK_{th} , which strongly affects both the Paris law exponent and the threshold stress intensity factor that describe fatigue crack propagation. Under the cyclic loading associated with fatigue, the continual fracture of the surface oxide layer formed at the crack front would enhance the effects of both the film rupture mechanism and hydrogen embrittlement. This continuous formation and then fracture of the surface oxide layer creates more opportunities for the corrosive environment to react with the crack front [17]. In aqueous environments, the fatigue crack growth rate is a function of the water vapor pressure and the time available for the material and environment to react [15].

During hydrogen embrittlement, the crack growth acceleration is attributed to the increase in the crack tip stress intensity produced by the buildup of hydrogen pressure in the internal voids ahead of the crack tip, illustrated in Figure 15. Like SCC, the presence of this high hydrogen concentration at the crack tip causes severely localized stresses and failure occurs when a critical strain is reached. In corrosion fatigue, the hydrogen influence [22] on crack growth is far more severe due to the cyclic loading because the fatigue process continually fractures the surface oxide layer, exposing a fresh metallic surface to react with constituents in the environment [15]. An aggressive aqueous environment increases oxide formation at the crack tip where these oxides can create a wedging force that result in a higher stress at the crack front due to the corrosive environment as opposed to the loading force. These combined effects make it more difficult to experimentally determine a real ΔK_{th} in a corrosive environment. There is a

profound shift in the dependence of ΔK , typically producing a reduced ΔK_{th} in aggressive environments, at least in the intermediate region where power law behavior is observed [34].

Sensitization also plays a role in corrosion fatigue testing of AA5xxx alloys. Holtz et al. found that at low R values (Figure 19), sensitization a negligible effect on the ΔK_{th} for the given environment but a minor effect on the Paris law exponent. In contrast, fatigue at high R values (Figure 20) showed a systematic effect of sensitization upon both the ΔK_{th} and Paris Law exponent, n , in an aqueous salt-water environment. The difference lies in the relationship between K_{max} and K_{ISCC} . Holtz et al. experimentally determined that when $K_{max} < K_{ISCC}$ as is the case when $R = 0.1$ then ΔK_{th} is not as dependent on sensitization as when $K_{max} > K_{ISCC}$, i.e. when $R = 0.85$ [12]. This finding is synonymous with the theory that increased sensitization results in higher corrosion rates which in turn means more oxide deposits at the crack front and higher minimum stresses

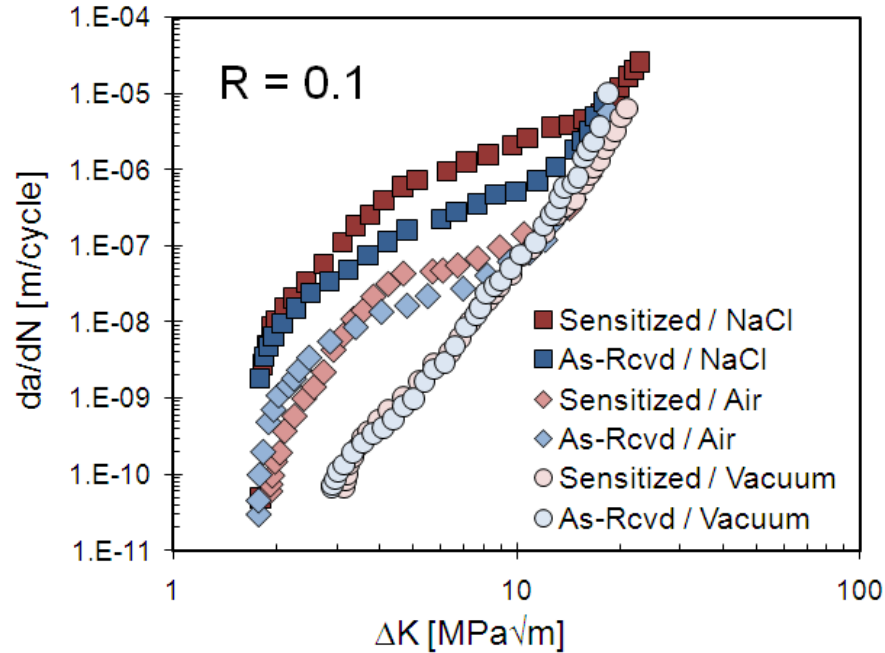


Figure 19. da/dN for $R = 0.1$ in Air, Vacuum, and Saltwater for As Received (R) and Sensitized (S) Samples. (From Holtz et al. [12])

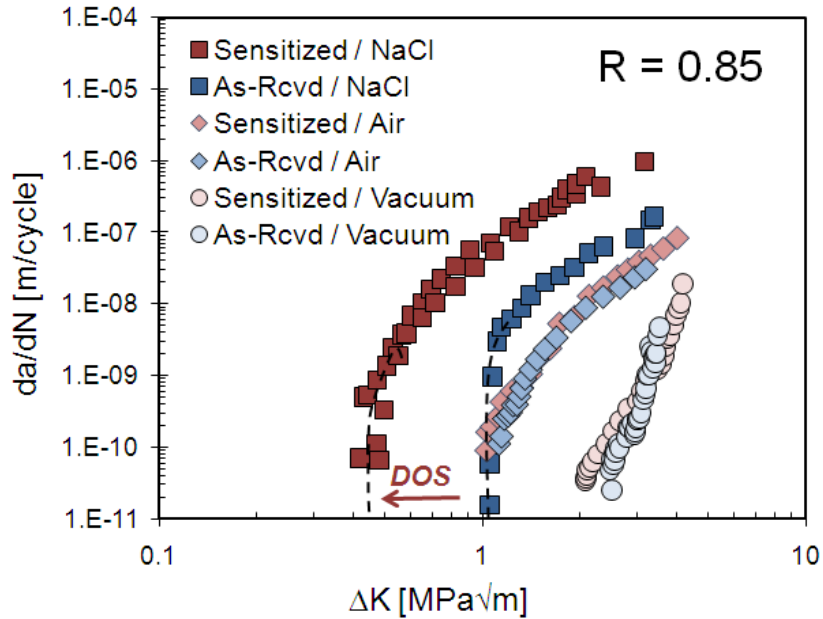


Figure 20. da/dN for $R = 0.85$ in Air, Vacuum, and Saltwater for As Received (R) and Sensitized (S) Samples. (From Holtz et al. [12])

Holtz et al. also found that changes in ΔK_{th} and n correlate directly to the β phase topology. Using the ASTM G67 nitric acid mass loss test to measure the degree of sensitization, Holtz et al. determined that around 30 mg/cm^2 , the anisotropic, semi-continuous microstructure is the most pronounced through TEM observations. The conclusion is that the transition from discontinuous to continuous grain boundary β phase is associated with changes in the corrosion fatigue behavior; specifically the critical mass loss for corrosion fatigue threshold degradation is 30 mg/cm^2 for AA5083-H116 [12]. Determining the critical mass loss value that correlates to the corrosion fatigue threshold degradation for AA5456-H116 would prove vital in the lifecycle management of this material on ships.

5. Mitigating Stress Corrosion Cracking and Corrosion Fatigue

There are many ways to combat stress corrosion cracking in marine environments, by either altering the properties of the building material or by some other means. In AA5456, decreasing the alloying Mg to below 3% would reduce the severity of sensitization and therefore the corrosion susceptibility would decrease. For example,

AA5454 has a nominal Mg content between 2.4 and 3.0 wt% with a yield strength of 12.0 ksi (82.74 MPa) in the H temper which is much lower than AA5456 with a yield strength of 37 ksi (255 MPa) in the H temper [8]. However, lowering the Mg content would significantly reduce the strength of the material therefore requiring more material to meet the strength demands and subsequently increasing the overall weight of the structure. The light weight and high strength combination is what made AA5456 a desirable material choice and, therefore reducing the Mg content is not an attractive option.

A second method for reducing corrosion cracking on marine vessels is applying paints and coatings. This method is currently in use but provides minimal protection against corrosion and should be used in addition to other protective methods. Any damage experienced by the surface coating reduces the integrity of the seal and will eventually result in base metal exposure. The small area of exposed aluminum would act as an anode while the larger protected area serves as a cathode resulting in a much faster corrosion rate on the exposed area.

Stress reduction, be it flexural as a result of the ship hogging and sagging, or residual caused by welds and rivets, is a third method for reducing corrosion cracking in marine vessels. It is impossible to remove the flexural stress experienced by a ship unless it is removed from service completely. Residual stress mitigation is an approach that is currently being widely researched [35–37]. The residual stresses surrounding a weld are tensile in nature. Improvements to basic welding practices, including fit up and edge preparation can reduce residual stresses around the weld area. Different welding techniques, such as friction stir welding (FSW), have also recently become a more effective way to weld materials susceptible to sensitization [38, 39]. FSW is a solid state process that does not melt the material during the joining process [40]. Since the heat input is less in this process, the residual tensile stress is less than the stresses experienced by materials that are welded by conventional means. The process of friction stir welding although effective, is large and not currently portable, making its use for shipyard repairs extremely difficult. While a viable option during initial construction, FSW is not yet available for repair and also does not solve the problem vessels that are already experiencing stress corrosion cracking.

Peening processes are another means of mitigating the tensile stress from welding by the addition of a residual compressive stress. There are several ways of adding residual compressive stresses by way of permanent plastic deformation to include ultrasonic impact treatment, shot peening and laser peening [40]. The effects of adding compressive stresses by means of shot peening and laser peening have proven to increase the fatigue limit of AA7075-T7351 in Figure 21 [8]. These are all developing processes and while most have been proven in controlled environments, the practical uses are limited by the size, cost, and mobility of the machines involved.

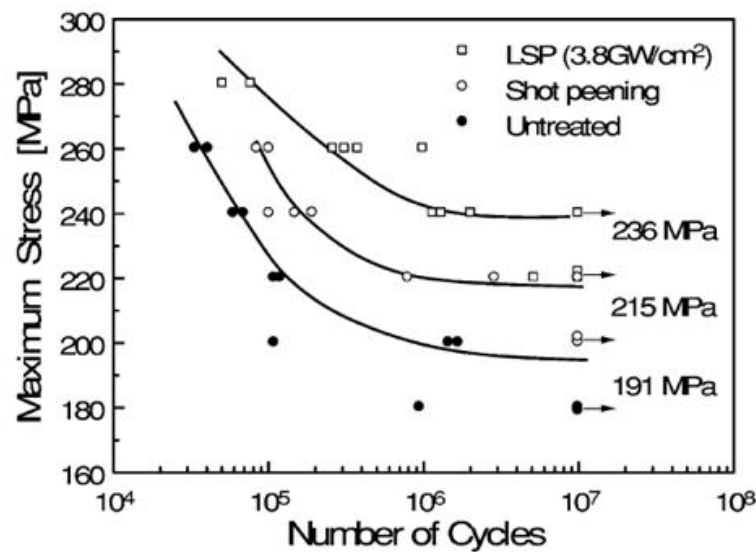


Figure 21. An S-N curve comparing the fatigue limit increases of 7075-T7351 aluminum alloy from shot peening and laser peening. (From Montross et al.[41])

C. THESIS OBJECTIVES

The purpose of this thesis is to characterize the stress corrosion cracking behavior of AA5456, both SCC and corrosion fatigue, as a function of sensitization. Before further research on how to mitigate SCC in AA5456 can be performed, the mechanical behavior of this material as it undergoes SCC must be first identified. The crack growth rates of other 5xxx series aluminum alloys in use on marine vessels, such as AA5083 have been previously characterized, however not on AA5456 [13]. As-received and sensitized samples of AA5456 were studied using static load tests to simulate SCC and

cyclic load tests to simulate corrosion fatigue in order to understand the effect of sensitization heat treatment on its mechanical properties in corrosive environments. Therefore the three objectives investigated by this thesis are:

Establish stress corrosion cracking methods at NPS.

Stress corrosion cracking is a new area of research at the Naval Postgraduate School. In order to investigate the SCC and corrosion fatigue behavior of aluminum alloys, we must first establish the necessary experimental capabilities to determine parameters such as K_{ISCC} and ΔK_{th} . With these methods in place and well established, the stress corrosion behavior of any material can be determined and methods for mitigating SCC can be explored.

Quantitatively determine the effect of sensitization on the slow crack growth behavior in AA5456

Our hypothesis is that the crack growth rates of AA5456 at increasing sensitization levels (i.e. higher mass losses) will be higher for AA5456 than for AA5083 given the larger amount of magnesium in the alloy. In addition, we expect that the K_{ISCC} value for AA5456 will be lower than for AA5083 for the same reason. These measurements are made by bolt-loaded, dual-cantilever beam fracture with intermittent exposure to salt water.

Quantitatively determine the effect of sensitization on the fatigue crack growth behavior in AA5456

Our hypothesis is that as sensitization increases, the fatigue life of AA5456 in salt water will decrease. We posit that the ΔK_{th} will decrease as a function of sensitization and be much lower compared to the as received material and less than the ΔK_{th} values for AA5083 identified in previous research.

THIS PAGE INTENTIONALLY LEFT BLANK

II. EXPERIMENTAL PROCEDURE

A. MATERIAL PROCESSING

1. Plate Fabrication

The material used in this thesis is the aluminum alloy 5456 with the heat treatment H116 provided by Sunshine Metals from Harvey, Louisiana. The AA5456-H116 was in the form of 8.0 x 36.0 inch plate that was 1.25 inches thick. The chemical composition of AA5456 is: magnesium 5.07, manganese 0.64, iron 0.181, silicon 0.114, chromium 0.085, titanium 0.0231, zinc 0.017, copper 0.012 and the remainder aluminum. The individual compositions are given in weight percent (wt%) and were certified by the American Bureau of Shipping.

Two different sample configurations were used for the following experiments. The double cantilever beams (DCB) in Figure 22 designed according specifications set forth in ASTM G168 were used for the static load SCC tests and single edge notch beams (SENB) designed in accordance with ASTM E399, shown in Figure 23 were used for the corrosion fatigue tests [42, 43].

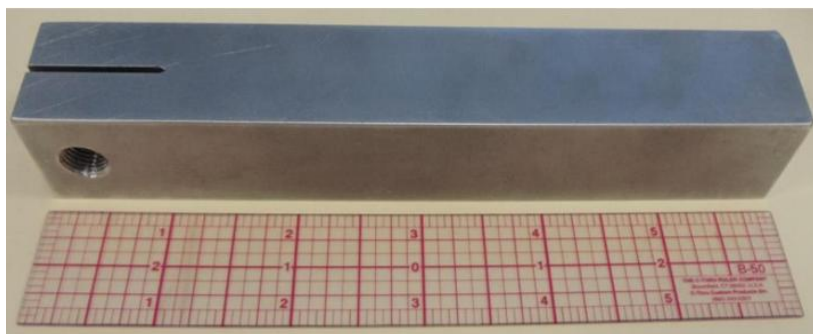


Figure 22. Double Cantilever Beam Test Specimen with ruler in inches

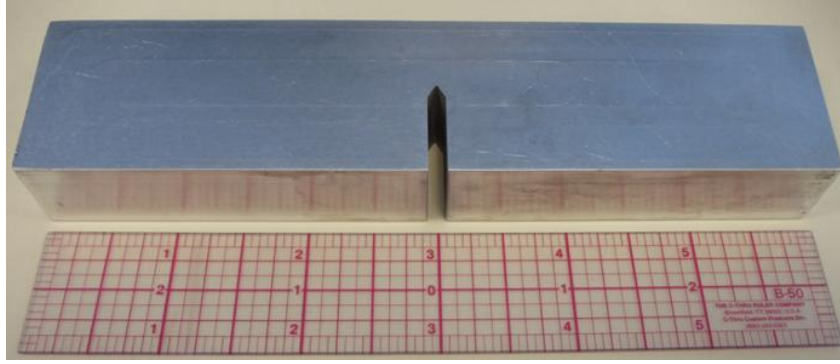


Figure 23. Single Edge Notch Beam Test Specimen with ruler in inches

From the stock plate, DCB samples were fabricated in the S-L orientation and SENB were fabricated in the T-L orientation, shown in Figure 24. These orientations were chosen based on numerous works that demonstrated that the orientations resulting in crack growth parallel to the rolling direction produced the most significant crack growth. [12-15, 20] Plate size and configuration prevented the SENB samples to be fabricated in this orientation; however, the T-L orientation has a similar relationship between the notch orientation and rolling direction and was used by Brosi and Lewandowski in air-fatigue measurements on AA5456 [14].

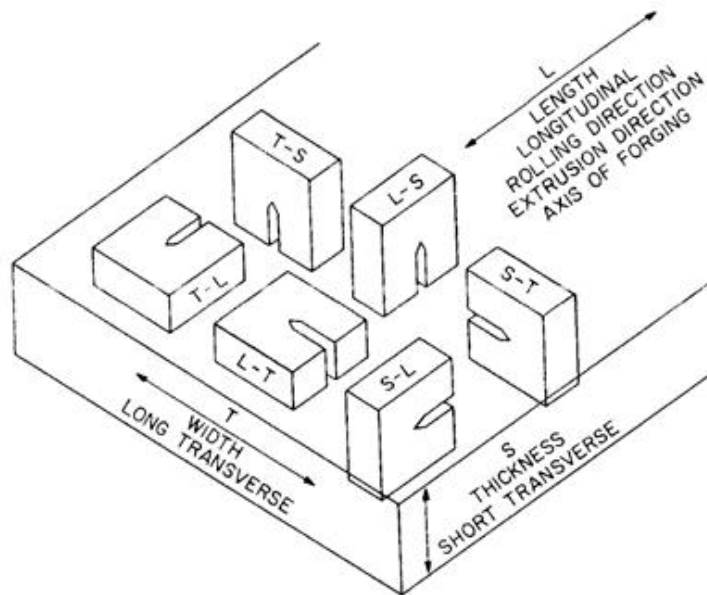


Figure 24. Specimen Orientation: DCB samples were fabricated in the S-L orientation and SENB were fabricated in the T-L orientation. (From ASTM E399, [43])

Both sample types were fabricated at Full Spectrum Machining Inc. in Gilroy, CA using the wire electrical discharge machining (EDM) process. This process was chosen due to the nature of the notch sensitivity, to ensure that crack initiation was possible, and to limit the heat input into the samples to avoid uncontrolled sensitization. The detailed view of the notch configuration used is illustrated in Figure 25 showing a Chevron notch crack starter with a tip angle of 60° . The required radius of the notch according to ASTM Standard E399 and G168 is 0.01" or less to ensure that the notch is sharp enough to initiate crack growth; this tolerance was achieved through the EDM process.

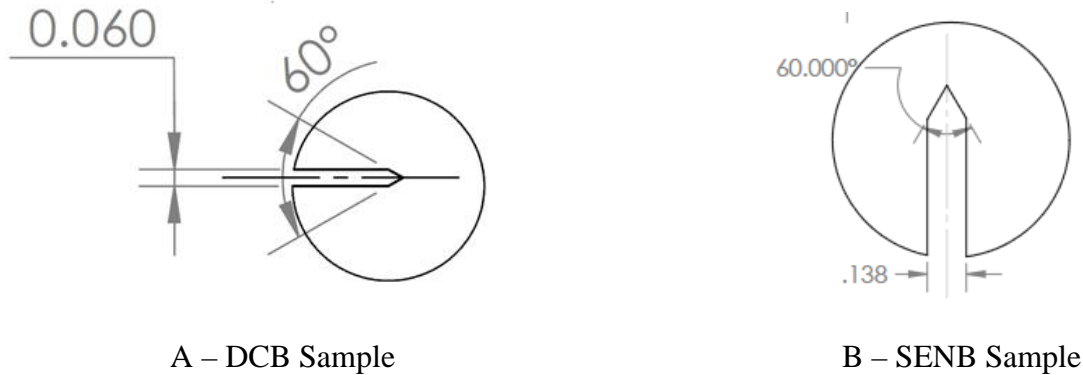


Figure 25. Detailed view of Chevron notch crack starter with dimensions provided in inches

2. Sample Sensitization and Preparation

Samples for both the DCB and SENB test configurations were aged by way of sensitization using an air furnace at a temperature of 175°C for four different lengths of time: 24, 168, 336, and 504 hours. No sensitization data for AA5456 was available; therefore the heating schedule for AA5083 was used as they are similar alloys [19]. This schedule was based on the work of Oguocha et al. who found that 175°C is the temperature, at which sensitization of AA5083 is a maximum.

The as-received and sensitized samples were progressively ground on the notched side using 240, 320, 400 and 600 grit sand paper to remove saw blade markings and other surface flaws. Following grinding, a 3- μm , oil based, diamond polishing suspension was used to polish the area around the notch tip to high smoothness. The purpose of grinding

and polishing was to remove surface flaws and create a polished surface where crack initiation and propagation would be easily identified and measured via optical methods. The samples were then thoroughly cleaned with methanol and dried.

B. STRESS CORROSION CRACKING – DUAL CANTILEVER BEAM (DCB)

1. Sample Geometry

Specimen dimensions were in accordance with ASTM G168[42] for the DCB sample, with top and side views shown in Figure 26. This geometry was designed to ensure that the plane strain conditions were maintained at the crack tip.

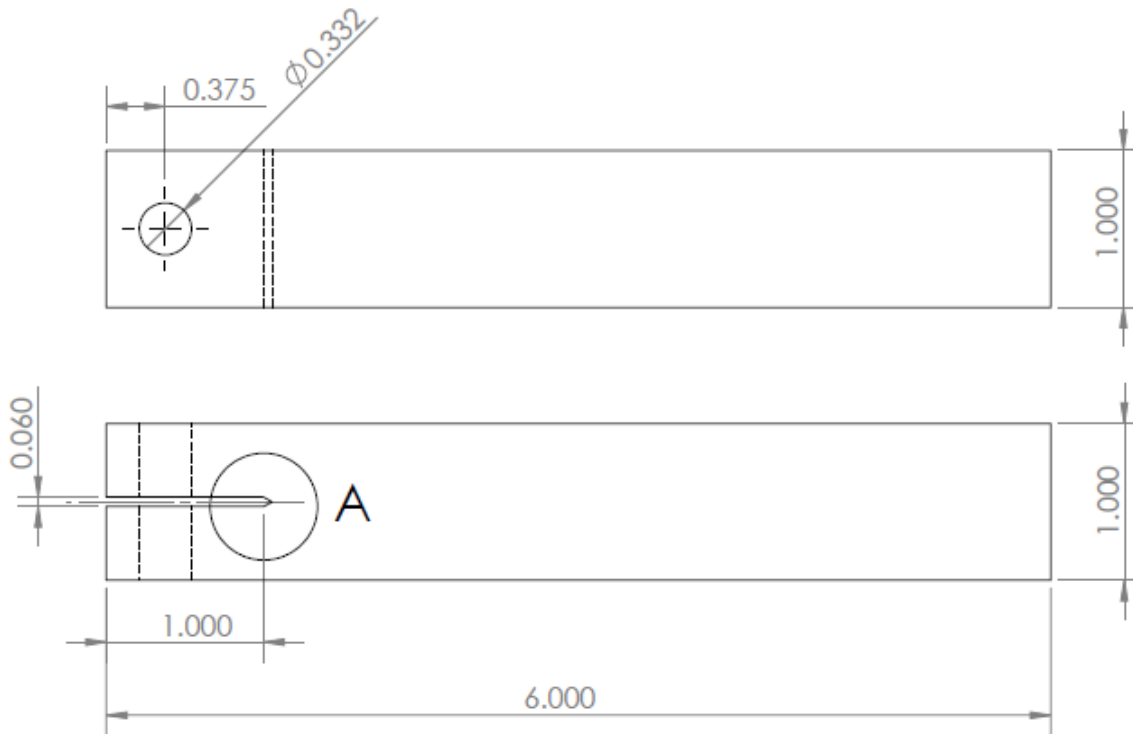


Figure 26. Top and side view of the plane strain DCB sample with dimensions provided in inches.

2. Pre-cracking

The DCB samples were first pre-cracked in air by way of sinusoidal cyclic loading using the MTS 858 loading frame with a 10 kN load cell, shown in Figure 27. MTS 647 Side-Loading Hydraulic Wedge Grips were used to avoid slipping and ensure that every sample was tested in the same position. Samples were loaded to ensure that

the loading axis was perpendicular to the notch tip to promote straight crack growth. A stress ratio of $R = 0.1$ and a 10 Hz loading frequency using a sine waveform was used with a detailed view of the DCB pre-cracking setup is in Figure 28. Pre-cracking was completed in two phases, crack initiation and crack propagation.



Figure 27. MTS 858 Machine

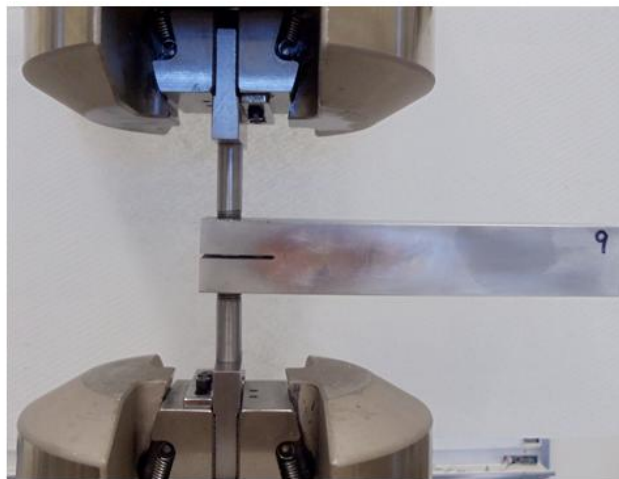


Figure 28. Detailed view of double cantilever beam pre-cracking setup in MTS

The purpose of the crack initiation phase was to produce a sharp, fatigue crack at the machined notch tip. The initial ΔK value for crack initiation was based on the desired target starting stress intensity factor (K_I) to be used during the salt-water exposure portion of the test. The desired K_I for the salt-water exposure was to be 14 MPa \sqrt{m} based on the work completed at ALCOA. Following ASTM Standard G168, the maximum stress intensity factor (K_{max}) used during pre-cracking is not to exceed $0.667K_{I0}$. Using the stated K_{I0} value of 14 MPa \sqrt{m} , the resulting K_{max} not to exceed is 9.388 MPa \sqrt{m} . Therefore a K_{max} of 9.16 MPa \sqrt{m} was first used to initiate crack growth. Loads inputted to the MTS 858 were calculated via spreadsheet based on the sample thickness, length, notch length and desired K value. First a P_{max} was determined based on the desired K_{max} . Then a P_{min} was calculated based on the R value and the mean and amplitude loads were calculated in Equations (18–19). For crack initiation, a mean load of 1.688 kN and an amplitude of 1.380 kN was used.

$$P_m = \left(\frac{P_{max} + P_{min}}{2} \right) \quad (18)$$

$$P_a = \left(\frac{P_{max} - P_{min}}{2} \right) \quad (19)$$

A second phase of pre-cracking was to propagate the initial crack outside of any plastic zone created by the cyclic loading at the higher ΔK . The fatigue crack propagation was stopped once the desired pre-crack length was reached. Fatigue conditions of $R=0.1$ and a $\Delta K = 6.24$ MPa \sqrt{m} were used until crack growth extended to a size of 2.5 to 3.8 mm from the tip of the machined notch. The mean load for crack propagation was 1.15 kN and the amplitude was 0.941 kN. The final pre-crack length (a_0) was determined by measuring the crack length on both surfaces and averaging the two values. Samples were not cleaned following pre-cracking to avoid contamination of the crack.

3. SCC Static Loading Test

Pre-cracked DCB samples were loaded by way of constant displacement using two Type 316 Stainless Steel bolts, 3/8 inch (9.525 mm) in diameter with 24 threads per

inch (TPI), or 0.98 threads per millimeter, shown in Figure 29. The high threads per inch were necessary to have maximum control when loading the samples. A bolt with 24 (TPI) will have one revolution result in 1/24 inch (1.058 mm) of linear travel. With a diameter of 3/8 inch (9.525 mm) and therefore a circumference of 1.178 inches (29.92 mm), the bolt will travel 0.035 inches (0.889 mm) per revolution. This linear travel distance directly correlates to the notch mouth opening meaning that the control over the distance the notch mouth opens is a function of the bolt threading and the higher the TPI, the finer the control on the notch displacement.



Figure 29. Type 316 Stainless Steel bolts, 3/8" (9.525 mm) in diameter with 24 TPI (0.98 threads per millimeter) used for static loading of DCB samples

The notch mouth opening (V_o) is the constant displacement used during this test and was calculated via Equation (20) where K_{IO} is the target stress intensity factor of 14 $\text{MPa}\sqrt{\text{m}}$, a_o is the starting crack length measured from the load line to the end of the pre-crack, C_o is the distance from the load line to notch opening, H is the half height, and E is the modulus of elasticity [42]. The dimensional values are illustrated in Figure 30. The loading bolts were tightened until the desired notch mouth opening displacement (V_o) was reached.

$$V_o = 2.309 \left(\frac{K_{IO}}{E} \right) H^{1/2} \left(\left(\frac{a_o}{H} \right) + 0.673 \right)^2 \left[1 + 1.5 \left(\frac{c_o}{a_o} \right) - 1.15 \left(\frac{c_o}{a_o} \right)^2 \right] \quad (20)$$

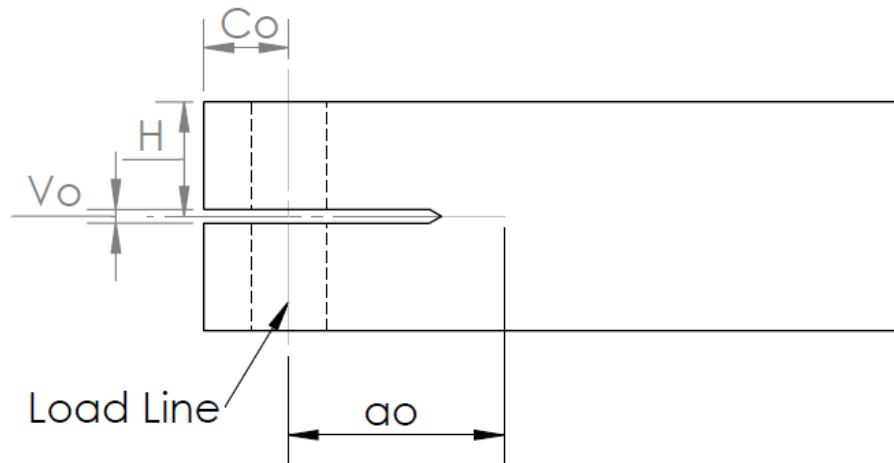


Figure 30. Illustration of measurements used to determine the notch mouth opening desired to facilitate SCC

The environmental testing conditions and application method were based on the work of Bovard [13]. A 3.5% NaCl solution was made from distilled commercial bottled water and table salt that did not contain iodine. Specimens were exposed to a 3.5% NaCl solution (salt water) via periodic drop-wise application of the solution. One dropper full of salt water, approximately 1 mL, was dropped down the notch of the sample allowing the liquid to collect at the root of the notch and seep into the crack as show in Figure 31. This process was repeated twice daily with salt water solution remade weekly.



Figure 31. Illustration of NaCl solution drop-wise application to double cantilever beam samples during constant loading test

Crack lengths were measured on both sides of the sample twice daily for the first week, daily for the second week, and twice a week for the remainder of the test time. The crack length was determined by averaging the lengths measured on each side. The test was carried out for 800 hours or 33 days. At the completion of the salt water exposure period, the DCB samples were again cyclically fatigued using the MTS 858 to extend the crack at least 1 mm further. A mean load of 6.0 kN and a load amplitude of 3.0kN was used to extend the crack to a reasonable length where cutting the sample would not affect the crack surface for analysis. The samples were then cut, crosswise with a band saw to expose the crack surface.

The final crack length, caused by corrosion, was measured on the fracture surface over five different points: the center of the crack front, halfway between the center and each side of the sample, and at each side of the sample. These five values were averaged to determine the final length of the corrosion crack.

The crack length versus time data was converted into crack velocity versus K_I data for analysis and comparison of the plateau crack velocities and K_{ISCC} determination

for each sensitization level. Crack velocity was determined by dividing the change in crack length by the change in time and K_I was calculated through Equation (21) [42].

$$K_{Ia} = \frac{(V_o E)}{\left\{ 2.309 H^{\frac{1}{2}} \left(\frac{a_o}{H} + 0.673 \right)^2 \left[1 + 1.5 \left(\frac{C_o}{a_o} \right) - 1.15 \left(\frac{C_o}{a_o} \right)^2 \right] \right\}} \quad (21)$$

C. CORROSION FATIGUE – SINGLE EDGE NOTCH BEAM (SENB)

1. Sample Geometry

Specimen dimensions for the SENB samples were in accordance with ASTM E399 and are shown in Figure 32. The sample was designed so that plane strain conditions were met at the crack front.

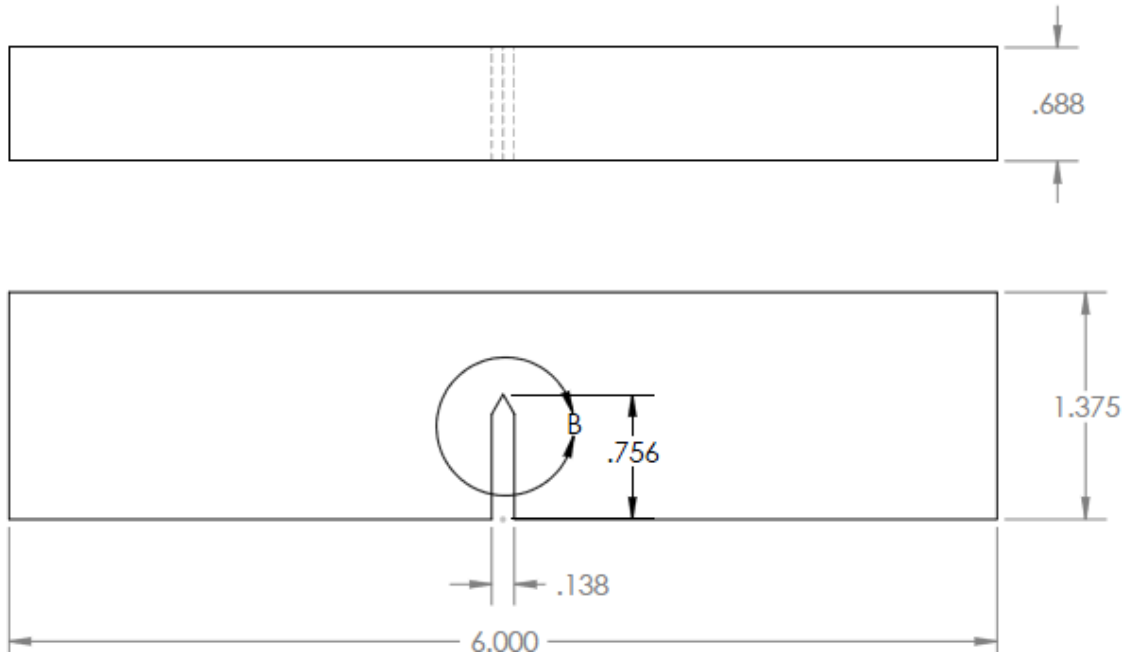


Figure 32. Top and side view of the plane strain SENB sample with measurements provided in inches.

2. Pre-cracking

The SENB samples were first pre-cracked by way of sinusoidal cyclic loading using the MTS 858 loading frame with a 10 kN load cell. A three point bend loading fixture, shown in Figure 31, was used with a span, S of 5.5 inches (139.7 mm). Two rollers were used on either end to allow for the specimen to move slightly under loading with the purpose of minimizing friction. The upper loading fixture was aluminum with a rounded edge to facilitate a narrow point load along the entire width of the specimen.

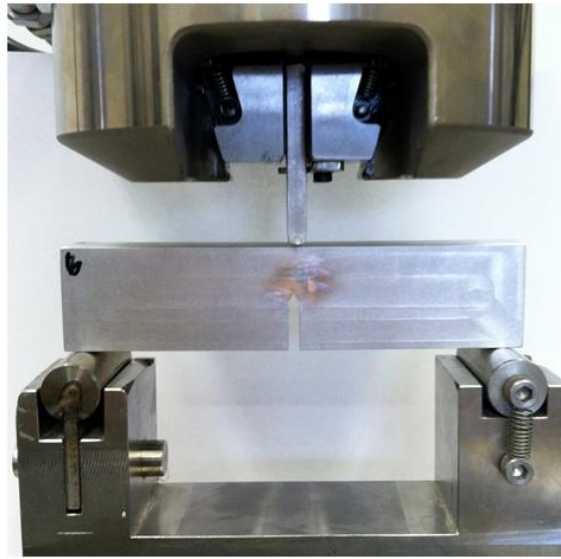


Figure 33. MTS 858 three point bend configuration used for SENB fatigue pre-cracking

Samples were pre-cracked in air in two stages, similar to the procedure for the DCB samples, using at 10 Hz loading frequency, a sine waveform, and a stress ratio of $R = 0.1$ for both stages. A ΔK of $9.75 \text{ MPa}\sqrt{\text{m}}$ was used first to initiate a crack of approximately 0.5 mm in length. The mean load used was -1.390 kN and with an amplitude of 1.138 kN. The ΔK was then reduced to $8.00 \text{ MPa}\sqrt{\text{m}}$ with a mean load of -1.141 kN and an amplitude of 0.934 kN. Samples were cycled until the crack extended past 1.3mm in length.

3. Increasing ΔK to Determine Threshold

Pre-cracked SENB samples were loaded cyclically in a salt water solution with increasing ΔK values until crack growth was observed. A 3.5% NaCl solution was made

from distilled commercial bottled water and table salt that did not contain iodine. Specimens were submerged (Figure 34) in the 3.5% NaCl solution (salt water) for the duration of the corrosion fatigue testing.

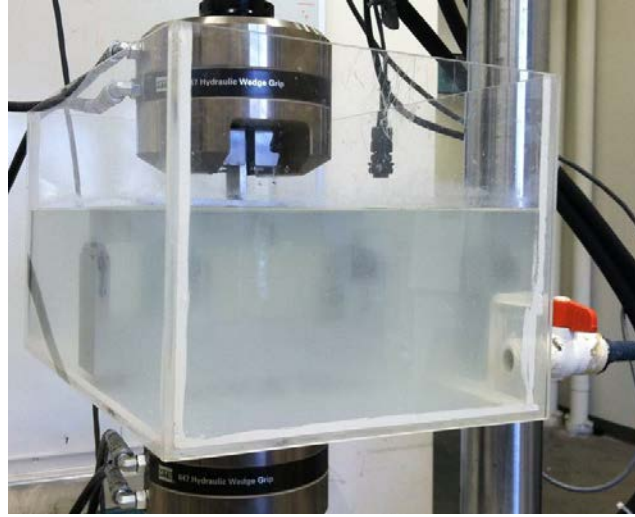


Figure 34. Tank used for submersion of SENB in three point bend corrosion fatigue tests conducted in 3.5 wt% NaCl

Samples were cyclically fatigued starting at a ΔK of 1.0 MPa \sqrt{m} with a loading frequency of 10 Hz and stress ratio of $R = 0.1$ for a duration of 400,000 cycles. At the conclusion of this test segment, if the crack growth did not grow 1mm then the test was repeated at a ΔK of 1.25 MPa \sqrt{m} . This process was repeated, increasing ΔK by 0.25 MPa \sqrt{m} until crack growth of 1mm was detected. A summary of the mean and amplitude loads used are in Table 5.

ΔK (MPa \sqrt{m})	Mean Load (kN)	Load Amplitude (kN)
1.00	-0.1431	0.1171
1.25	-0.1786	0.1461
1.50	-0.2141	0.1751
1.75	-0.2495	0.2042
2.00	-0.2850	0.2332

Table 5. Summary of mean and amplitude loads used for ΔK threshold corrosion fatigue tests.

D. NITRIC ACID MASS LOSS TEST – ASTM G67

The nitric acid mass loss test was conducted in accordance with the ASTM G67 standard.[9] The nitric acid (HNO_3) was reagent grade with a specific gravity of 1.42 (71 wt%) and the 5 % sodium hydroxide (NaOH) solution used for etching was also reagent grade. The water used for preparing the NaOH solution and rinsing the samples was distilled commercial bottled water.

The samples used were 1 in x 1 in x 1 in (25.4 mm x 25.4 mm x 25.4 mm) and were cut using the Buehler Isomet 200 precision saw from the sensitized and as received DCB specimens. The sample surfaces were lightly ground with 600 grit sand paper to remove surface impurities while maintaining the integrity of the as-fabricated surface. Samples were scribed for identification purposes and to identify the rolling direction.

The ratio of sample surface area to volume of nitric acid required is 19 mL/in² (30 L/m²) [9]. The surface area was determined to be 6 in² ($3.81 \times 10^3 \text{ m}^2$) therefore requiring 114 mL of nitric acid per sample. First, samples were etched by submerging them in the 5 % NaOH for 1 min. They were then rinsed in distilled water and then desmutted to remove the reaction products caused by etching from the surface of the material through submersion in nitric acid for 30 seconds. The samples were rinsed with distilled water a final time and allowed to air dry. They were then weighed and submerged in 114 mL of nitric acid in individual glass containers for 24 hours. After the test was complete, the samples were removed, rinsed with distilled water and allowed to air dry before weighing them a second time. The mass loss of each sample was calculated by finding the difference in the two masses per unit surface area to the nearest whole number, mg/cm².

E. MICROSTRUCTURAL ANALYSIS

1. Fracture Surface Characterization

The fracture surfaces of the fractured DCB samples were characterized to determine the final SCC length and the characteristics of the corrosion crack surface. The samples were cut crosswise through the second fatigue crack region (after the SCC) and across the notched region to produce samples that contained the fatigue pre-crack, the SCC region, and the second fatigue crack. This geometry allowed for the analysis of

both the onset of SCC and the final corrosion crack front. Samples were ultrasonically cleaned using the Buehler Ultramet 2005 Sonic Cleaner for 10 minutes in methanol and then dried with a hot air gun. The samples were mounted on a circular holder for fracture surface analysis. The Zeiss NEON 40 field emission gun scanning electron microscope (FEG-SEM) was used for fracture surface characterization. A working distance between 5.0mm and 5.5mm was used along with an accelerating voltage of 2.00 kV. The secondary electron detector, located at an angle of 54° from the vertical was used to collect the images.

2. Crack Surface Characterization

The cracked DCB samples were cut using the Buehler Isomet 200 precision saw, isolating the SCC for analysis. The surface containing the crack was metallographically prepared in a standard fashion using a number of steps (Table 6). The first step was to grid the samples using a Buehler Ecomet 4 Variable Speed Grinder-Polisher. The Sample surface was ground using a succession of finer grit silicon carbide sandpapers, starting with 1200 grit and finishing with 4000 grit. Each grit was applied to the sample surface in increments of 10 minutes at 140 rpm. Between each grit level, the sample was rinsed with water and methanol.

Next, the samples were polished using a Buehler Ecomet 3 Variable Speed Grinder-Polisher. This process was completed in three steps. First a 3 μ m Buehler MetaDi monocrystalline diamond suspension solution was used for 5 minutes at 130 rpm. This was followed by a 1 μ m Buehler MetaDi monocrystalline diamond suspension solution for 5 minutes at 130 rpm and finally a 0.05 μ m Buehler Mastermet Colloidal Silica Polishing suspension solution was used for 5 minutes at 130 rpm. Between each step, the samples were rinsed with water and methanol. Following polishing, the samples were ultrasonically cleaned using a Buehler Ultramet 2005 Sonic Cleaner for 10 minutes in methanol, dried with a hot air gun and stored in a vacuum chamber.

Step	Process	Time	RPM
1	1200 Grit SiC Paper	10	140
2	2400 Grit SiC Paper	10	140
3	4000 Grit SiC Paper	10	140
4	3 micron MetaDi Diamond Suspension	5	130
5	1 micron MetaDi Diamond Suspension	5	130
6	0.05 micron Colloidal Silica	5	130

Table 6. Grinding and Polishing Conditions

F. HARDNESS MEASUREMENTS

1. Hardness Tests

Hardness measurements were made to investigate the effects of sensitization on the hardness of the aluminum. Rockwell hardness was used to measure changes in hardness at the four sensitization levels and the as-received sample. Three different orientations with respect to the plate rolling direction were tested: S, T, and L, shown in Figure 35. Each surface was lightly ground using 600 grit sandpaper to create an even surface finish. The hardness measurements were made on the Rockwell B scale using a 100kg load with a 16mm diameter steel ball as the indenter. Five hardness tests were performed on each of the three surfaces on each sample.

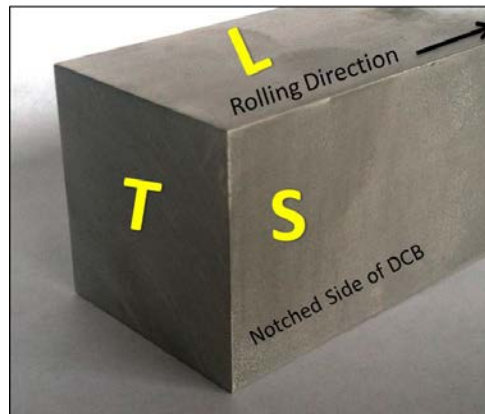


Figure 35. Orientation of sensitized and as received DCB sample Rockwell B hardness tests.

THIS PAGE INTENTIONALLY LEFT BLANK

III. RESULTS AND DISCUSSION

A. MASS LOSS TEST (ASTM G67)

1. Mass Loss Results

The results of the ASTM G67, nitric acid mass loss test conducted on the four sensitized and as received samples are shown in Table 7. The as-received sample showed a minimal mass loss of 1 mg/cm², as expected, and mass losses increased as sensitization time increased. The ASTM standard indicates that mass losses over 25 mg/cm² are susceptible to intergranular corrosion therefore all of the samples sensitized for 24 hours or longer at 175°C are susceptible.

Sensitization Time (hrs)	Mass Loss (mg/cm ²)
0	1
24	30
168	62
336	63
504	64

Table 7. Mass loss of as received and sensitized AA5456-H116 after ASTM G67 nitric acid mass loss test

The samples sensitized for 168 h, 336 h, and 504 h, all exhibited similar mass losses with only a difference of 2 mg/cm² between the three samples. With a mass measurement precision of ± 0.5 mg and an area measurement precision of $\pm 10^{-3}$ cm², the measured mass loss of these three samples can essentially be considered to be the same. The graph in Figure 36 illustrates a plateau of mass loss as sensitization time increases. The sensitized samples also demonstrated a significant change in color after the nitric acid exposure, shown in Figure 37. Samples that were sensitized for 336 h and 504 h also showed visible manifestations of the grain boundary attack on the surface of the samples by way of aluminum flakes and surface exfoliation shown in Figure 38.

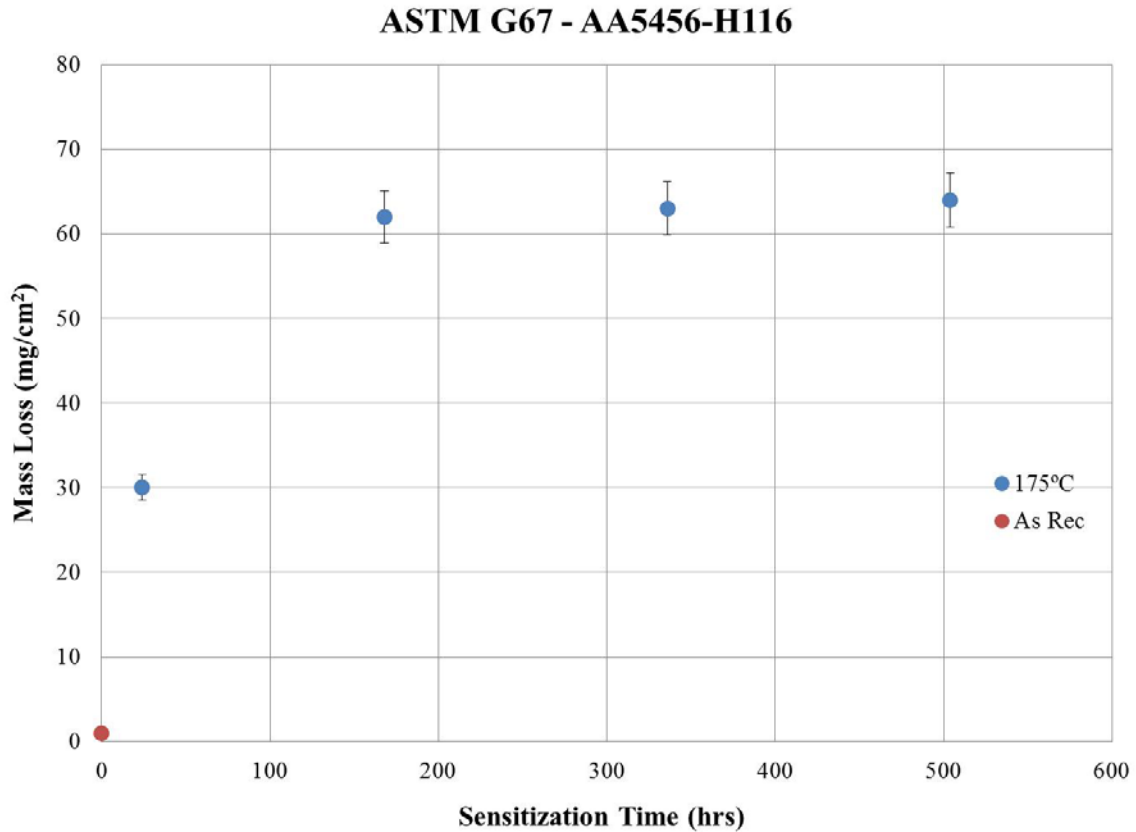


Figure 36. Nitric Acid Mass Loss Test (ASTM G67) for AA5456-H116 showing mass loss as a function of sensitization time.



Figure 37. NAMLT for as received and sensitized samples showing a difference in color between the two. Samples are 1 inch on each side.

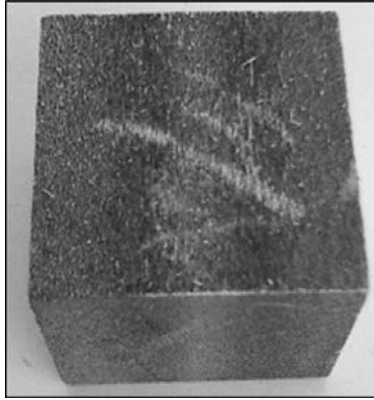


Figure 38. Surface flakes and exfoliation present on AA5456-H116 sample sensitized for 336 hour and subject to ASTM G67, nitric acid mass loss test. Sample is 1 inch on each side.

2. Mass Loss Comparison with AA5083

The mass loss associated with sensitization in the AA5456-H116 samples was higher for all sensitization levels compared to the mass loss for the same aging time and temperature for AA5083-H131 [13]. There was no measureable mass loss associated with the as-received samples for AA5456-H116 however, as received samples of AA5083-H131 did have a mass loss of 2.2 mg/cm^2 [13]. Figure 39 shows that the AA5083-H131 exhibits mass loss after only one hour of sensitization at 175°C while the AA5456-H116 shows virtually no mass loss in the as received condition. This indicates that AA5456-H116 is less susceptible to IGSCC in the as received condition than AA5083-H131.

For longer aging times, AA5456-H116 exhibited higher mass losses than AA5083-H131 with a plateau in sensitization occurring for exposures over 150 hours. An aging time of 150 hours produced a mass loss of 60 mg/cm^2 for AA5456-H116 while the same aging time and temperature produced a mass loss of about 47 mg/cm^2 for AA5083-H131 samples. The mass loss of the AA5456 samples plateaued for subsequent aging times; however the mass loss of AA5083-H131 continued to increase. AA5083-H131 showed the same asymptotic characteristics but for aging times much longer than 150 hours (over 1200 hours).

Mass loss data for AA5456-H116 was also compared to AA5083-H116 in Figure 40. The comparison of these materials is important because while they have the different

magnesium contents, the temper is the same. Opposite to the findings for AA5083-H131, both alloys in the H116 temper showed almost zero mass loss in the as received condition. This relationship between the mass losses of the two aluminum alloys is significant because while AA5456-H116 shows less susceptibility to IGSCC than AA5083-H131 in the as received condition, it is the same as AA5083-H116.

For a sensitization time of about 150 hours, AA5083-H116 showed a mass loss of 110 mg/cm², which is much higher than the mass loss of 62 mg/cm², observed with AA5456-H116. However, at shorter sensitization times, for example 24 hours, the AA5083-H116 had a mass loss of around 15 mg/cm², which is half the mass loss AA5456-H116 at the same sensitization time. It can be concluded that sensitization has a much more aggressive impact on the H116 temper for both alloys at sensitization times above 100 hours compared to AA5083-H131. It can also be concluded that the temper of the material and not the Mg content has a greater effect on the mass loss, and therefore the degree of sensitization, of 5xxx series aluminums.

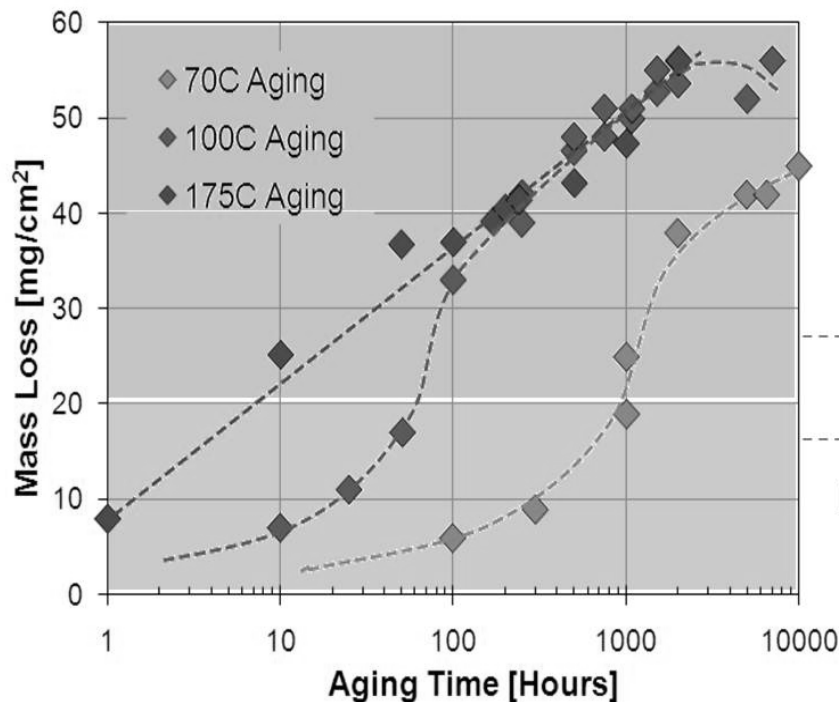


Figure 39. ASTM G67 NMLT results showing mass loss for AA5083-H131 as a function of aging time and temperature. (From Holtz et al. [12])

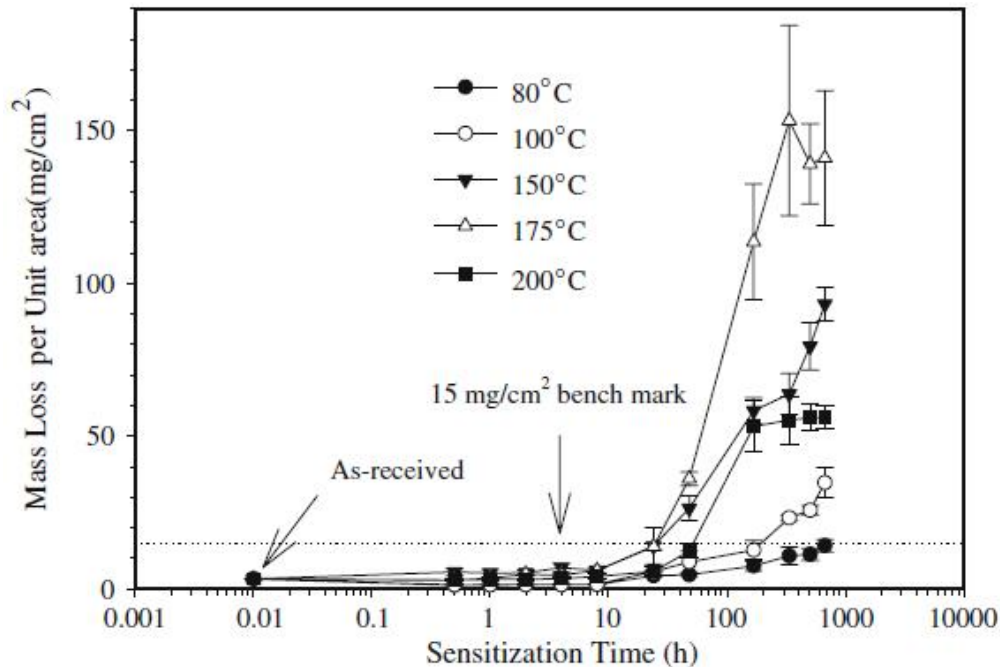


Figure 40. ASTM G67 NAMLT results for AA5083-H116. (From Oguocha et al. [19])

Mass losses or degree of sensitization can be directly correlated to the weldability of the material using the scale in Figure 41 as the assessment on the weldability of sensitized aluminums. AA5456-H116 samples that were sensitized over 150 hours all had a mass loss over 60 mg/cm^2 and are therefore not weldable while AA5083 remains weldable for aging times well over 1000 hours at 175C. The AA5083 can remain in operation up to 6.7 times longer than AA5456 using this metric. Additionally, the aging time is dramatically decreased to 24 hours or less for welding 'as-is' for AA5456 meaning that the cost of welding AA5456 once the material is put into service will be much greater than AA5083 in almost all cases.

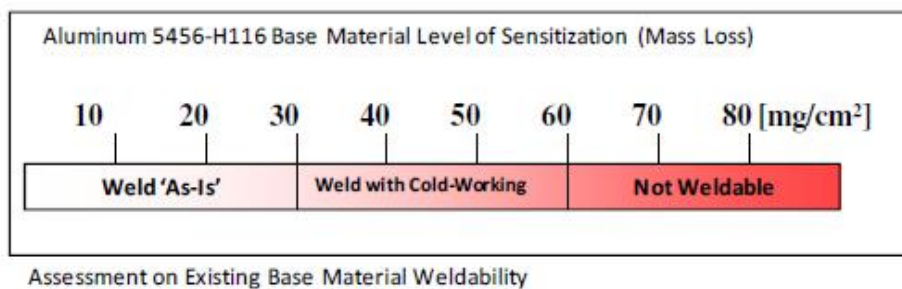


Figure 41. Assessment on existing base material weldability as a function of mass loss. (From Wong, [44])

The base plate thickness used for the mass loss samples in this work is 1.25 inches (31.75 mm), thicker than the base plate used in the literature. The differences in plate thickness result in possible differences in the microstructure of the material tested. The AA5456-H116 base plate from which samples were cut was 1.5 inches (38.1 mm) thick, while the AA5083 samples used for mass loss comparison was produced from 0.25 inch (6.35 mm) plate. During cold working, the microstructure in the center of the thicker plate is different from the microstructure closer to the surface of the plate due to the change in distance to the rollers used. A thinner plate results in a more isotropic material because the cold working effects reach the entire through thickness of the plate. Because dislocation networks can influence the kinetics and spatial distribution of beta phase formation, it would be important in the future to compare sensitization kinetics between alloys from plates of identical thicknesses.

B. HARDNESS

1. Rockwell B Hardness Results

The results of the Rockwell B hardness tests conducted on AA5456-H116 are illustrated in Figure 42. The hardness of the material decreases as sensitization time increases with an exponential decay. The hardness plateau begins around a sensitization time of 150 hours with a sharper decrease in hardness for lower sensitization durations.

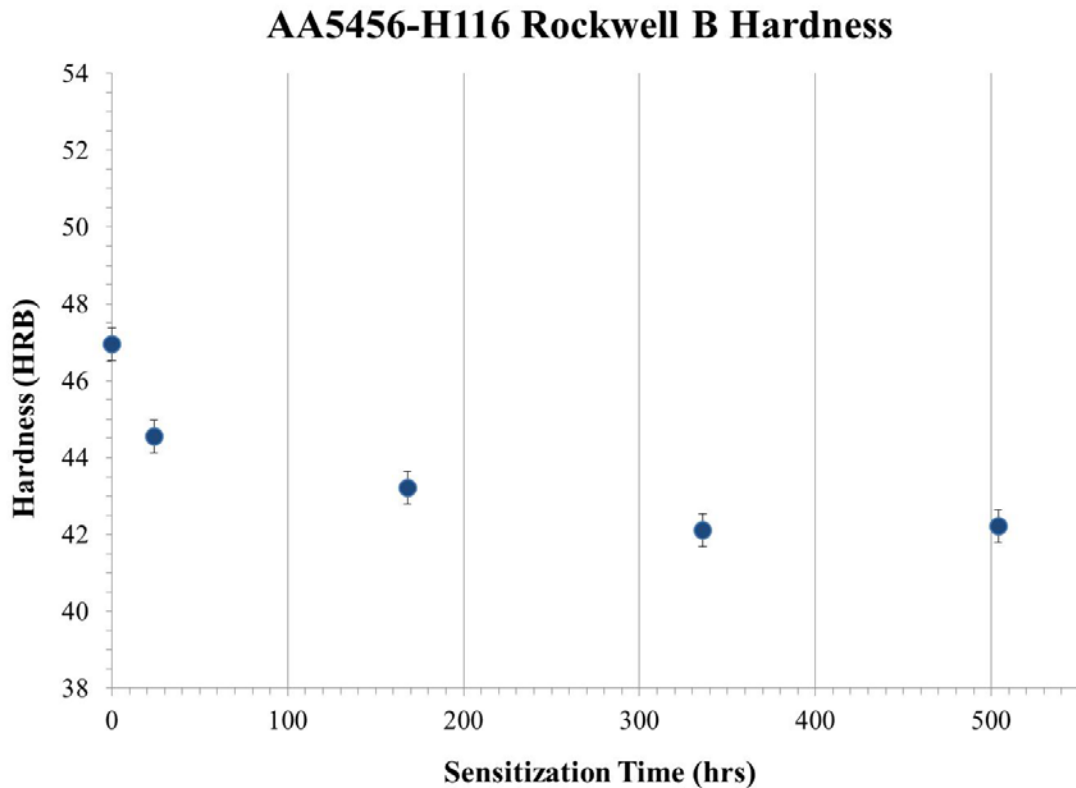


Figure 42. Effect of sensitization on Rockwell B hardness of AA5456-H116

Hardness data was also collected as a function of orientation with respect to the rolling direction. The data in each orientation as a function of sensitization time shows the same exponential decay relationship as the overall hardness of the material. Within each aging condition, there was a difference in hardness relative to the rolling direction of the plate from which the sample was taken. There was little change in the hardness in the S-direction, while in the L and T directions there was a marked decrease in hardness however. The hardness values in the L and T directions were statistically indistinguishable. The relative hardness also reversed as a function of sensitization at aging times greater than 168 hours. For minimal sensitization, the hardest direction was the T-direction, while for the higher sensitization time, the S-direction was the hardest.

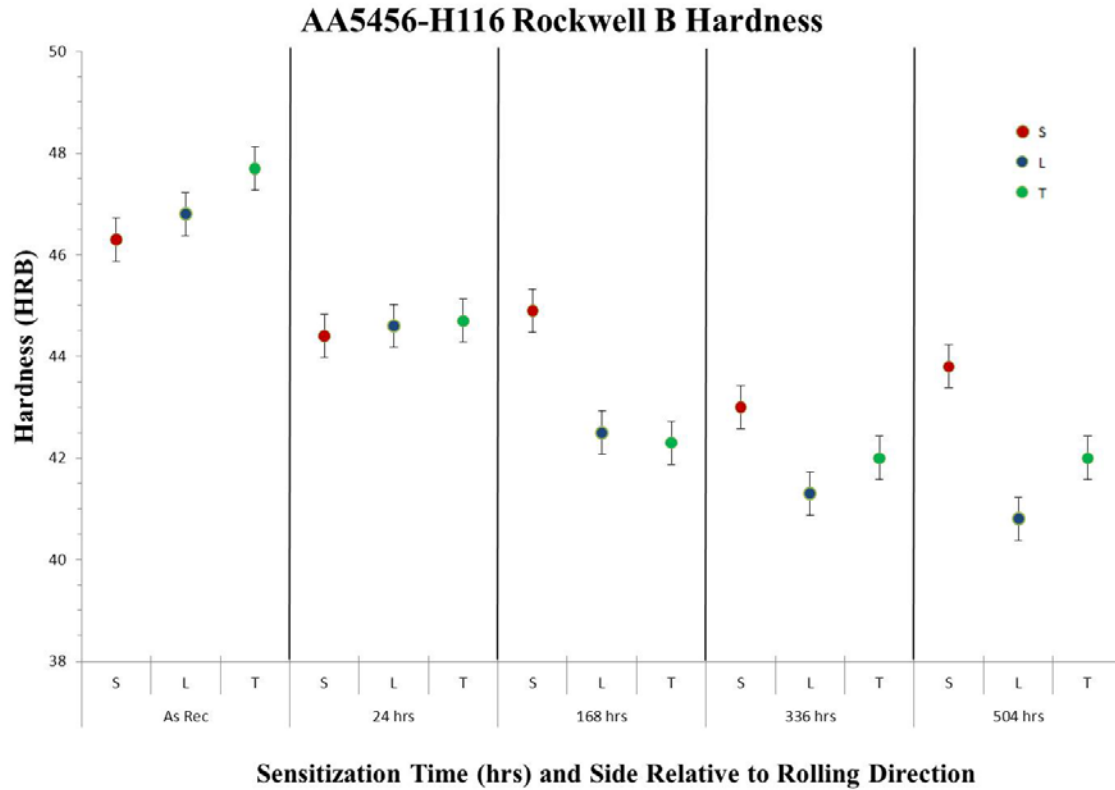


Figure 43. Effect of thermal conditions on Rockwell B hardness on AA5456-H116 relative to rolling direction

2. Comparison with AA5456-H116 Hardness in Literature

Compared to the Rockwell B hardness data collected on the same material, the values of the AA5456-H116 material sampled followed the same hardness trend as a function of sensitization however the actual values measured were much lower. Data collected by Brosi et al. in Figure 44 indicates that a decrease in hardness occurs as sensitization time increases up to 100 hours for a sensitization temperature of 175°C. The data for the lower sensitization temperatures of 80°C and 100°C in Figure 44 illustrate the same trend observed in Figure 42, a decrease in hardness up to 100 hours and a subsequent increase in hardness for sensitization times past 100 hours however, there is no data for the 175°C sensitization temperature past a duration of 100 hours for comparison. Brosi et al. attributed this increase in hardness at longer sensitization times to recrystallization of the material due to a longer annealing time. Hardness data can also

be compared to Vickers hardness data collected by Oguocha et al. on AA5083-H116 in Figure 45. This data showed that for AA5083 there was also an overall decrease in hardness as sensitization time increases.

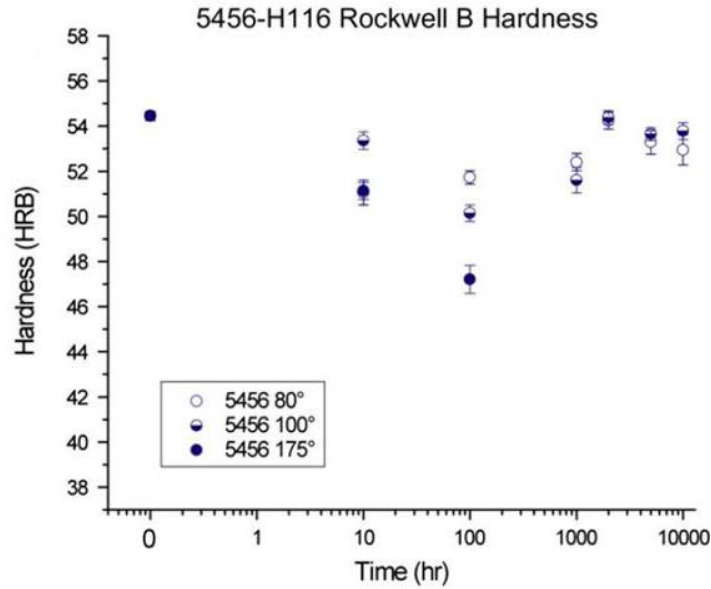


Figure 44. Effect of thermal conditions on Rockwell B hardness on AA5456-H116. (From Brosi et al.[14])

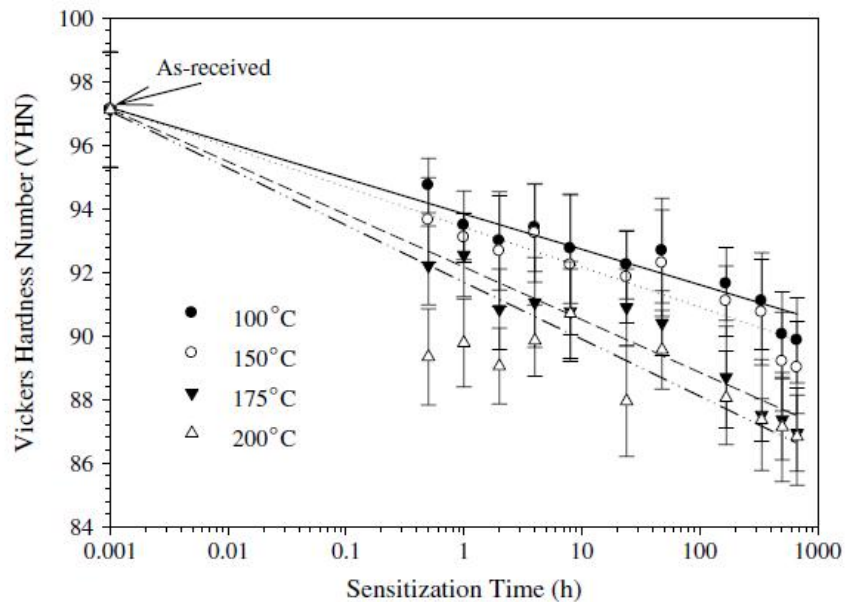


Figure 45. Vickers hardness measurements as a function of sensitization time for AA5083-H116. (From Oguocha et al. [19])

C. STRESS CORROSION CRACKING

1. DCB Constant Displacement SCC Crack Growth Rate Test Results

Crack growth rate and crack velocity data collected for AA5456-H116 exhibit the same trends as data collected on AA5083. The crack growth rate results of the statically loaded, double cantilever beam stress corrosion cracking test are illustrated in Figure 46. The lowest mass loss, associated with the as-received material showed very little crack growth over the duration of 30 days with a final crack length extension of only 1 mm. Crack growth rates of the sensitized material had a logarithmic trend with the highest level of sensitization corresponding to the sharpest increase in initial crack growth. The longest crack at the conclusion of the 30 day period was produced in the sample with the highest sensitization. The final crack lengths in the other samples decreased as the measured mass loss decreased.

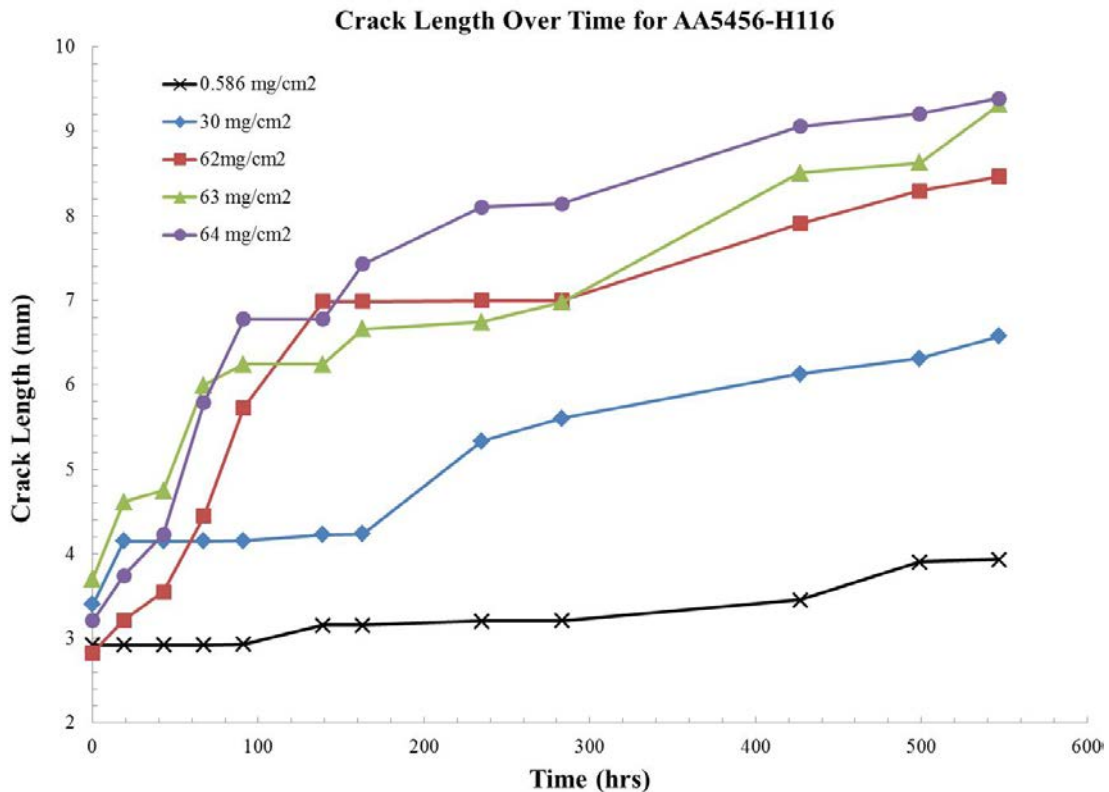


Figure 46. Data for measured crack length in millimeters versus time in hours for AA5456-H116.

The method for measuring the final crack length was to fatigue the sample past the SCC region and then fracture the sample to reveal the fracture surface. The five points used to measure the final crack length are illustrated in Figure 47. This final crack length measurement differed from the measurements taken during the test in that only the visible crack length on the sides of the sample were measured. As the crack front was not completely straight during growth, the crack length measurements taken from the sides of the specimen, during the test, were determined to be underestimates of the actual crack length.

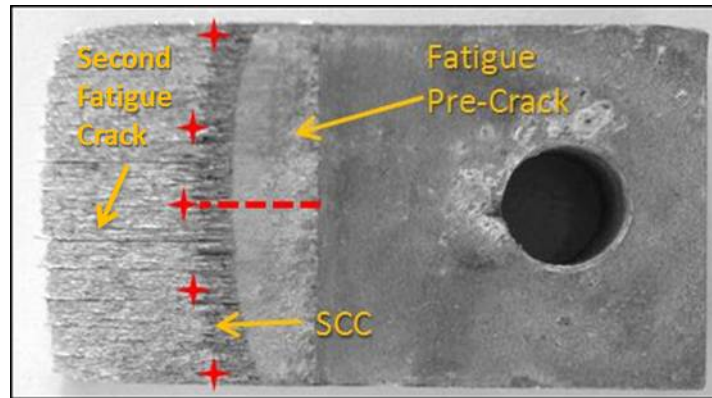


Figure 47. Final stress corrosion crack length measurement locations for DCB samples

From the crack length versus time data, the relationship between crack velocity and the applied stress intensity factor was computed (Figure 48). This plot presents three clear groups of data, the as received sample with a mass loss of a 0.586 mg/cm^2 , the sample with a mass loss of 30 mg/cm^2 , and the samples with 62 mg/cm^2 and 64 mg/cm^2 mass loss. The as-received material with a mass loss of 0.586 mg/cm^2 , produced the slowest crack velocity and the highest stress intensity factors. Both the velocity range and stress intensity range were an order of magnitude lower than the samples with the highest level of sensitization. The next highest sensitization level of 30 mg/cm^2 , resulted in a higher crack velocity and lower K values required for growth than the material with 0.586 mg/cm^2 mass loss. The final group of data, the samples with mass losses of 62 mg/cm^2 and 64 mg/cm^2 , presented the fastest crack velocity and lowest K values required for growth out of the samples tested. While the stress intensity, K_I , during SCC growth decreased appreciably as sensitization increased, there were no clear thresholds present in

the data. The plateau SCC velocity also increased as degree of sensitization increases with a plateau velocity in the range of 10^{-2} mm/hr for the 30 mg/cm² sample and 10^{-1} mm/hr for the 62 mg/cm² and 64 mg/cm² samples. These values correlate to the rate at which the crack propagates and therefore it can be stated that as sensitization time increased, crack velocity increased, and the window of detection before failure becomes smaller.

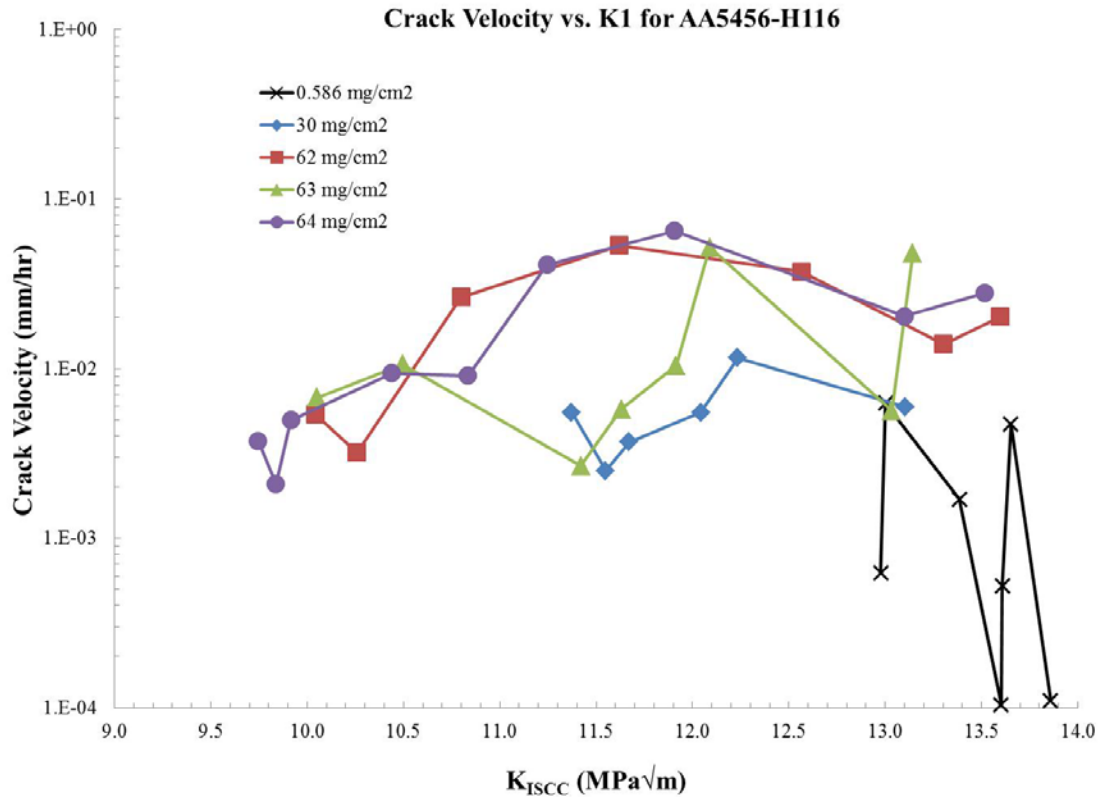


Figure 48. Calculated data for crack velocity in mm/hr versus K_I for AA5456-H116

2. AA5456-H116 Crack Growth Rate Comparison with AA5083

To determine the effect of additional Mg in AA5456 on the SCC growth rate, a comparison was made with the crack growth rate of AA5083 DCB samples subjected to similar environmental conditions. Data on AA5083 collected by Bovard showed similar trends to what was observed for AA5456-H116, however due to differences in the sample geometry, temper, and sensitization schedules, a direct comparison was difficult to make

[13]. For both AA5456-H116 and AA5083, as the degree of sensitization increased, the initial crack growth rate increased, before the crack growth rate in all samples reached a relative plateau.

K_{ISCC} data for AA5083-H131 as a function of mass loss was determined by Holtz et al. with a general trend in the data showing that as mass loss decreased, K_{ISCC} increased. After 800 hours, the range of K_I values for the data collected on AA5456-H116 was still above what was found by Holtz et al. however, the data in this study did not produce clear thresholds. To determine clear threshold values for AA5456-H116, an additional test that continued for longer than 800 hours would need to be conducted.

Several lessons were learned during the establishment of these tests. Specific SCC testing details were learned and will prove useful for further application of these tests. For AA5456, we were unable to “pop-in” a pre-crack without fatigue. In addition, it was noted that ensuring that the pre-crack length extended past the plastic zone created in the initial fatigue pre-cracking stage was crucial for reliable SCC growth measurements. The validity of optically measuring the crack length on the side of the specimen is suspect, especially when crack branching in the stress corrosion region starts with the addition of delamination and a loss of planarity of the crack front. This observation presents the question of how well stress corrosion cracks can be assessed in real life ship structures. If the majority of the crack propagation is occurring below the surface of the material and extends past the visible crack front, it may be difficult to determine the extent of the stress corrosion damage. Further error analysis needs to be conducted to determine accuracy of optical measurement of the crack growth on the sides of the samples.

C. CORROSION FATIGUE ΔK_{TH} DETERMINATION

1. SENB Corrosion Fatigue Results

Fatigue tests in air were conducted on an as received sample at Fracture Technology Associates (FTA) resulting in the da/dN curve in Figure 49. For a decreasing ΔK test, indicated by the open circles in Figure 49, the ΔK_{th} for this material can be identified to be $2.7 \text{ ksi}\sqrt{\text{in}}$ which is equivalent to $2.96 \text{ MPa}\sqrt{\text{m}}$. Threshold values

can be compared to the nearly identical data collected by Brosi et al. who determined that the ΔK_{th} tested in air with a loading ratio of $R = 0.1$ for as received AA5456 to be 2.8 ksi \sqrt{in} (3.07 MPa \sqrt{m}). The work by Holtz et al. in Figure 50 indicates that AA5083-H131 has a ΔK_{th} of about 1.9 MPa \sqrt{m} in air. The increase in ΔK_{th} by about 1 ksi \sqrt{in} (1.09 MPa \sqrt{m}) can be attributed to the increase in Mg content as well as microstructure due to different tempers. A change in the cold work applied to the materials will result in changes in dislocation density and other microstructural changes resulting in a change in the fatigue threshold.

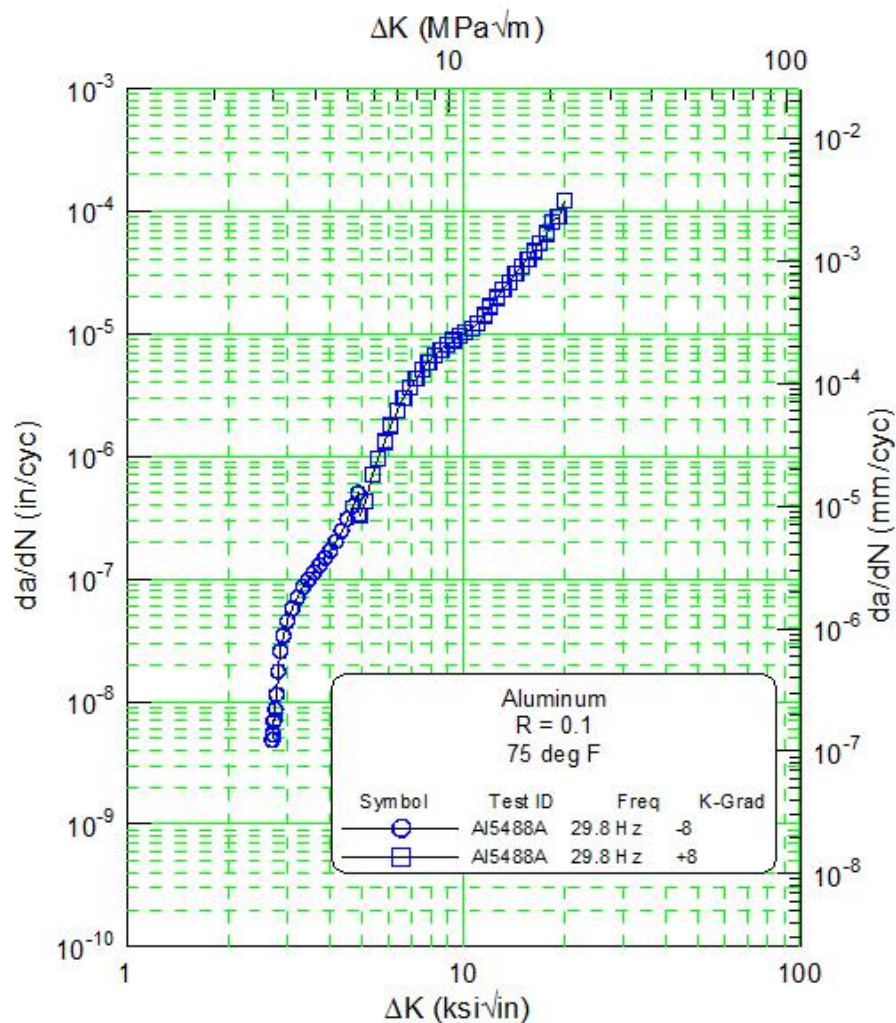


Figure 49. da/dN data collected on as received AA5456 sample at Fracture Technology Associates

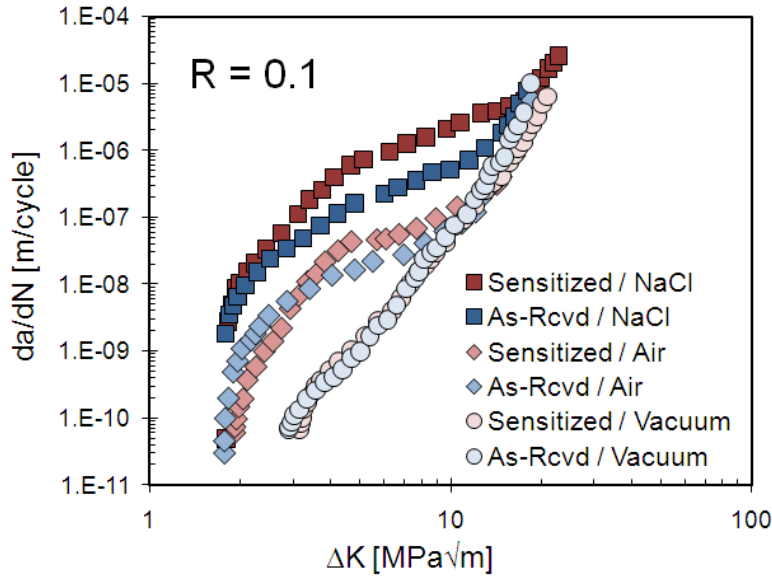


Figure 50. Fatigue of AA5083 in 1% NaCl, Air, and Vacuum of samples sensitized at 175°C for 200 hours and in as received condition with $R = 0.1$. (From Holtz et al. [12])

AA5456 corrosion fatigue samples were successfully pre-cracked in air and underwent successive increases in ΔK in salt water at a loading ratio of $R = 0.1$ until $\Delta K = 3.2 \text{ MPa}\sqrt{\text{m}}$, and at a loading ratio of $R = 0.85$ until $\Delta K = 1.5 \text{ MPa}\sqrt{\text{m}}$. Corrosion fatigue tests in salt water resulted in no visible crack growth for both loading ratios.

D. MICROSTRUCTURAL ANALYSIS

1. SCC Propagation Mode in DCB Samples

The results of the microstructural analysis on the crack profile and cross-section fracture surfaces revealed distinct changes between fatigue and SCC propagation modes, as a function of sensitization. In Figure 51a., the-as received sample showed little difference in the crack surface morphology between the fatigue pre-crack and the SCC regions with the only evidence of corrosion being the void at the tip of the crack front. For the sample with a 30 mg/cm^2 mass loss, the stress corrosion cracking surface crack extended further and secondary cracks, branching off from the main crack were clearly visible (Figure 51b). The secondary cracks are first noticed at a crack length of 4.5 mm, corresponding to a K_I of $12.88 \text{ MPa}\sqrt{\text{m}}$. Finally, for the sample with 62 mg/cm^2 mass

loss, a significant increase in the number of secondary cracks was observed (Figure 51c). The secondary cracks appeared much earlier along the main crack and to a higher degree at tip of the crack front than the sample with a mass loss of 30 mg/cm^2 . The first instance of secondary cracks occurred at a crack length of 2.5 mm, which marked the end of the fatigue pre-crack. There are several other secondary cracks found along the entire crack length; however, the first instance of major branching occurs at a crack length of 6.2 mm which correlates to a K_I value of $11.3 \text{ MPa}\sqrt{\text{m}}$. There is also evidence of pitting and general corrosion on the surface of this material with was not seen on samples that were sensitized to a lesser degree.

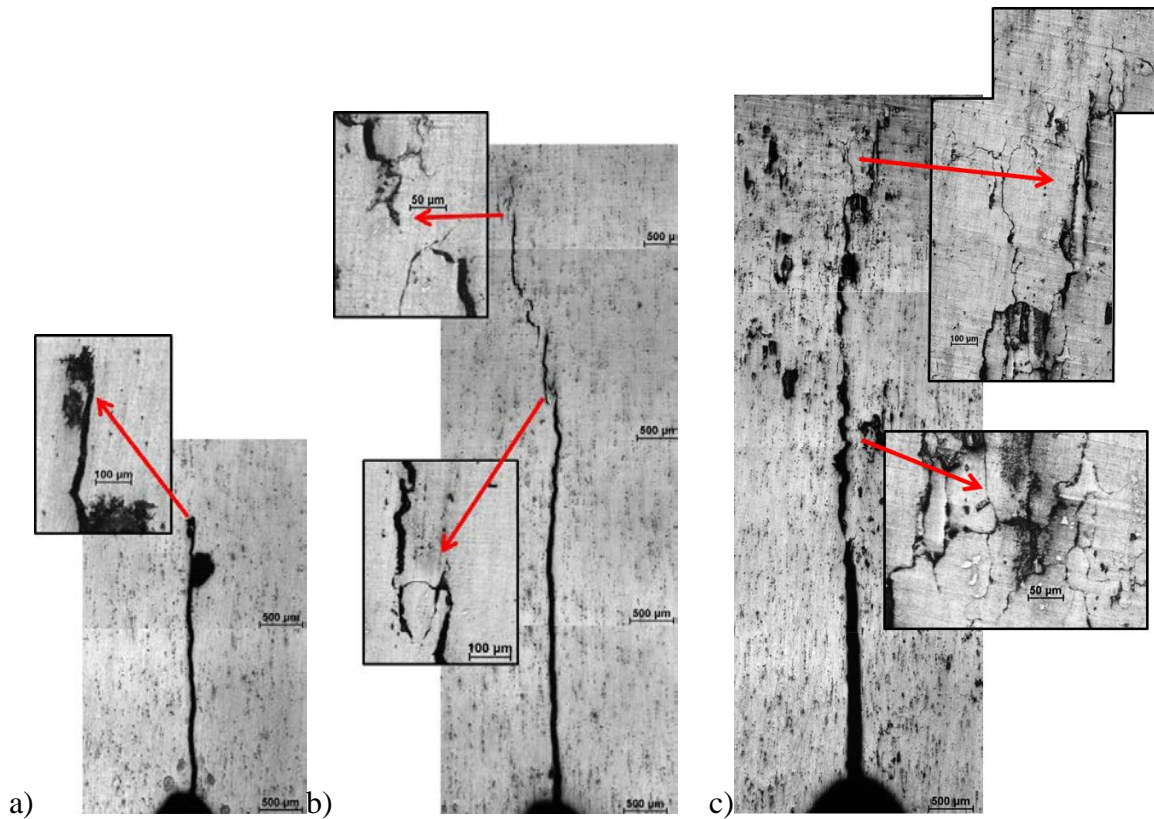


Figure 51. Crack Propagation modes in statically loaded DCB samples subject to SCC with varying mass losses due to sensitization. a) As received (0 mg/cm^2) b) 30 mg/cm^2 c) 62 mg/cm^2

The sample in Figure 52 is a fractured DCB sample that was sensitized for 336 hours with a mass loss of 63 mg/cm^2 . The sample is viewed end-on, or perpendicular to the primary fracture surface. The fracture surface shows that while the primary SCC cracking front occurred in the L, or longitudinal direction, (parallel to the rolling

direction); substantial secondary cracking occurred perpendicular to the main crack front in the S, or short transverse direction (parallel to the loading direction). There is also evidence of secondary cracks in the S-direction on these samples that do not appear to correlate to the main crack plane. These secondary cracks do not seem to connect to the two dimensional crack that propagated from the stress corrosion crack plane (that was initiated by the fatigue pre-crack) but form independently. This observation could mean that at levels of sensitization this high (in the not weldable regime) applied stresses result in IGSCC both along a main crack but also spontaneously within the material.

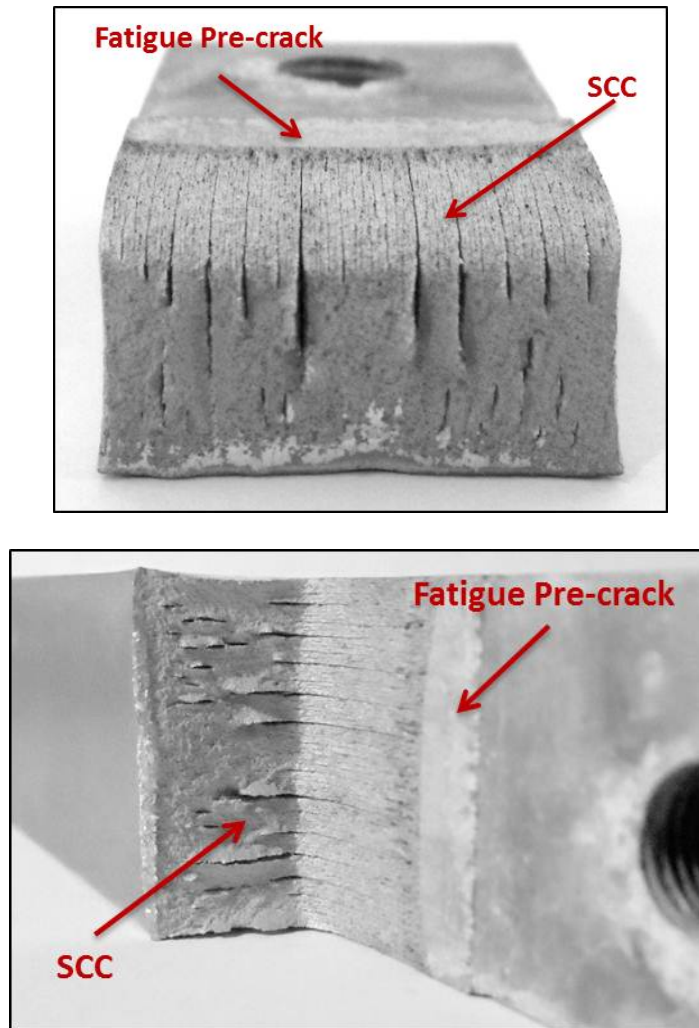


Figure 52. Secondary Cracks in AA5456-H116 DCB Samples with a mass loss of 63 mg/cm² after being subjected to static bolt loaded SCC test

Scanning Electron Microscope (SEM) images were taken from the primary fracture surfaces for samples at the three sensitization levels of 0 mg/cm², 30 mg/cm² and 63 mg/cm². The image in Figure 53 depicts the fatigue pre-crack region on the top and the SCC region below. There are small SCC cracks extending from the fatigue pre-crack that propagate in two directions but the SCC region is very small overall. The SEM image in Figure 54 is for the sample with a mass loss of 30 mg/cm², and it shows a significant increase in the number of two-dimensional cracks and a much more pronounced SCC region. Wide “fingers” of stress corrosion cracks propagate past the main crack front in all of the sensitized samples. These “fingers” create an uneven crack front, as opposed to the uniform crack front created by the fatigue pre-crack. The unevenness of the SCC propagation region reveals that the stress corrosion cracks propagate at different rates within the microstructure. Additionally, the SEM images show that these crack extensions are three-dimensional, a morphology that can be correlated to the corrosion tunnel model. According to theory, these tunnels grow in diameter and length as a function of microvoid coalescence, where the varying propagation rates are a function of the microvoids are created through the preferential corrosion of the β -phase on grain boundaries. Crack propagation is slower through the grains themselves in this theory, therefore substantiating the uneven nature of the stress corrosion crack front. The sample with a mass loss of 63 mg/cm² in Figure 55 shows a much more even crack front however, secondary two-dimensional cracks are much more prevalent and much longer than the samples with less mass loss.

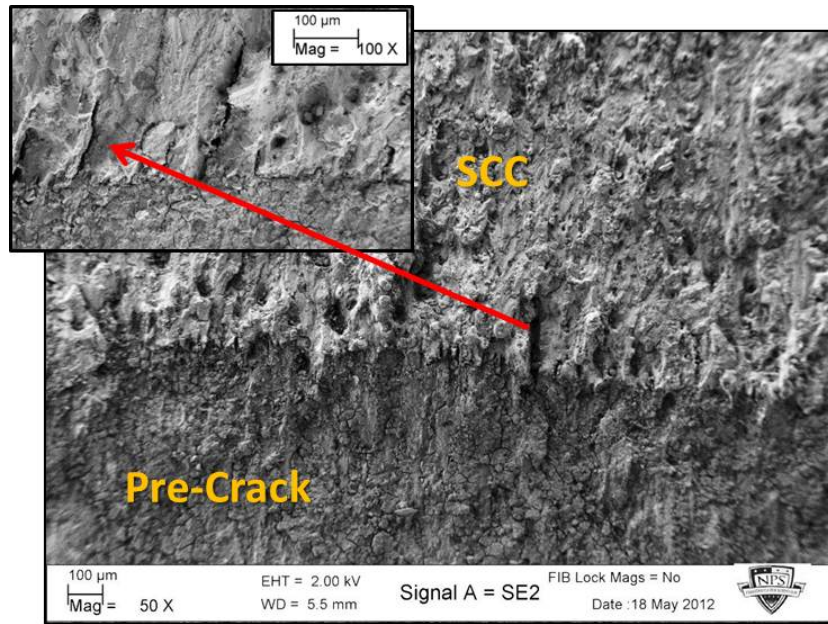


Figure 53. SEM images depicting SCC crack initiation characteristics for a statically loaded DCB sample of the as received material with 0 mg/cm² mass loss. The red arrow indicates a magnified image of the small stress corrosion cracks observed.

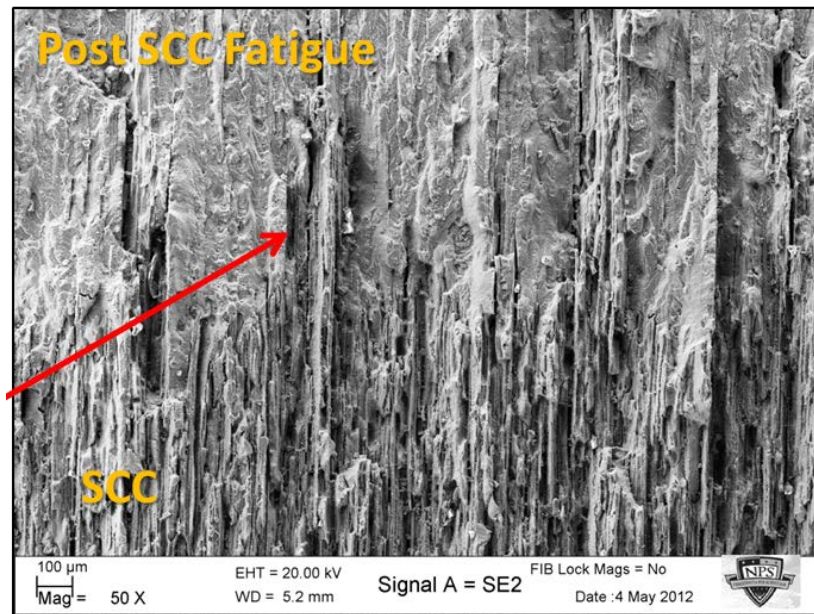


Figure 54. SEM image depicting SCC crack front characteristics for a statically loaded DCB sample aged at 175°C for 24 hours with a mass loss of 30 mg/cm² and arrow indentifying a crack front indicative of the corrosion tunnel model for SCC propagation.

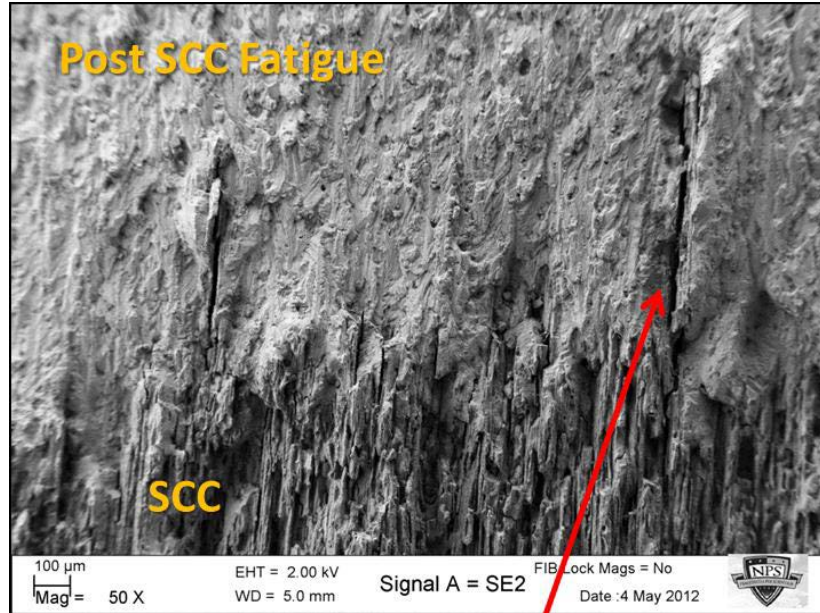


Figure 55. SEM image depicting SCC crack front characteristics for a statically loaded DCB sample aged at 175°C for 336 hours with a mass loss of 63 mg/cm² and arrow indicating the presence of two dimensional crack.

2. Comparison of Fracture Surfaces with AA5083

Work by Brosi et al. on the delamination of fatigue cycled AA5456-H116 found longitudinal splitting in sensitized samples that were fatigued in air. The splitting, or secondary cracks were attributed to transverse stresses that resulted in fracture along grain boundary regions weakened by the evolution of grain boundary precipitation [14]. Evidence of splitting and secondary cracks was not present in the fatigue pre-crack or overload fatigue region (post SCC) in the samples in the current work and the work by Brosi et al. due to the high K values used to form the pre-crack or break the sample. The overloading of stresses in this region during both fatigue processes results in the creation of a large plastic zone in the material thus preventing delamination from occurring. Brosi et al. observed delamination in fatigue samples at lower K values that were sensitized for at least 100 hours at 175°C and subject to a K_{\max} of 11 MPa√m or more. The same observations were made in the current work, where all statically loaded DCB samples were subject to a $K_{\max} = 14.0$ MPa√m. Samples in the as received condition and those that were sensitized for 24 hours did not exhibit secondary cracks, while samples that had been sensitized for 168 hours or longer did have secondary cracking.

Secondary cracks were also found in three dimensions in samples of AA5083, tested in salt water by Bovard et al. shown in Figure 56. These cracks were both parallel and perpendicular to the fatigue pre-crack showcasing the same characteristics of the secondary cracks observed in the current work.

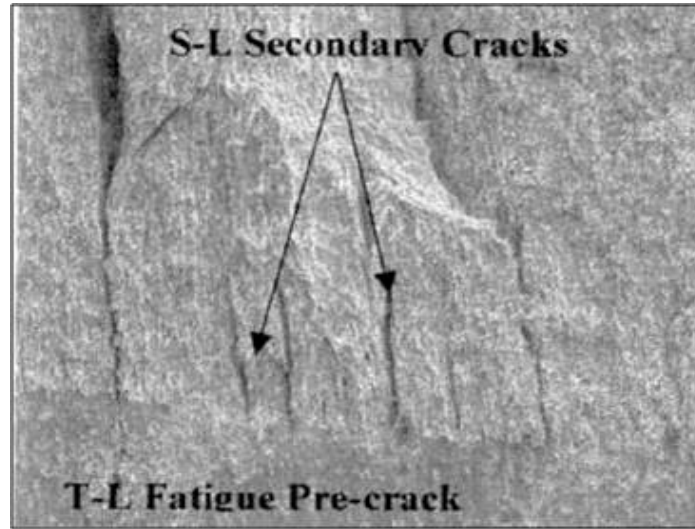


Figure 56. Secondary Cracks in SCC fracture surface for AA5083. (From Bovard,[20])

F. FUTURE WORK

The development of corrosion fatigue and SCC test methods at the Naval Postgraduate School is the foundation for future work in the characterization of materials and the mitigation of stress corrosion cracking in the U.S. Navy. Specifically, future work on corrosion fatigue with the implementation of instrumentation such as a clip-on gage for measuring ΔK during SENB fatigue testing will result in the accurate determination of ΔK_{th} in a salt water environment. The ultimate goal would be to create a comparison of the relationship between ΔK_{th} and K_{ISCC} for AA5456 and then compare the results with the relationship between these two values for AA5083 as shown in Figure 57.

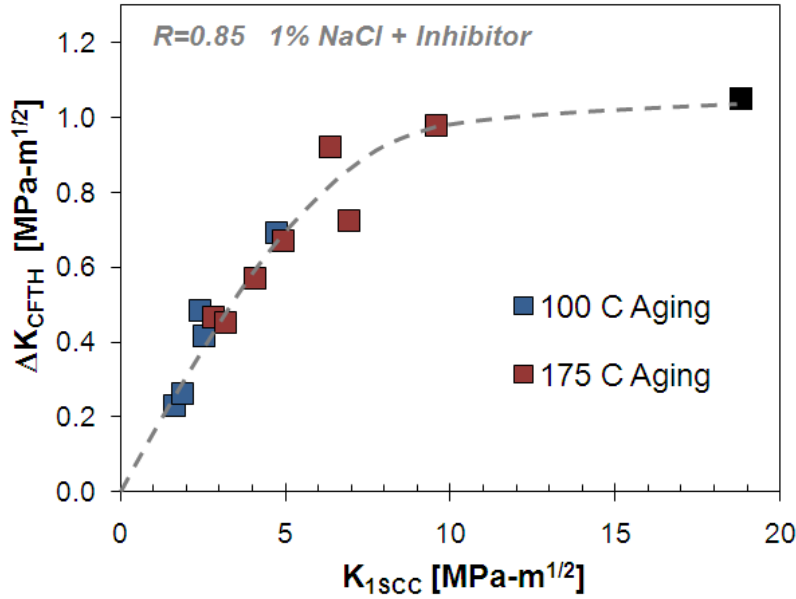


Figure 57. Relationship between ΔK_{th} and K_{ISCC} as a function of mass loss for AA5456. (From Holtz et al. [12])

Additional instrumentation would also help improve data collection on the statically bolt-loaded DCB, stress corrosion cracking tests. Instrumented bolts would provide continuous and automatic measurement of the crack length through a measured change in compliance. This automated measurement is important, particularly for submerged testing, as it does not depend upon the ability of the research to visually see the crack to measure its length. The surface of the samples quickly oxidized and made visually measuring crack length difficult as the testing progressed. Ultrasonic measuring techniques provide an additional means for measuring crack length during SCC testing. Ultrasonic measuring techniques would provide imaging of the entire crack front as opposed to measuring each side of the samples.

The sensitization levels that were used during this research resulted in three of the samples having similar degrees of sensitization, while gaps in the data existed for lower degrees of sensitization. Repeating testing using sensitization times between 24 hours and 168 hours would result in a more complete picture of the effects of sensitization on mass loss, hardness, and K_{ISCC} .

Finally, developing a test to determine the effect of laser peening for mitigation of SCC in AA5456 would prove useful. The purpose of investigating the SCC characteristics of this material is not only for the prediction of failure but for the prevention of SCC failure in materials currently in use on both commercial and naval ships. To prevent future costly repair overhauls, an effective way to lengthen the life of the material in use would save money while still maintaining a reliable structure.

THIS PAGE INTENTIONALLY LEFT BLANK

IV. CONCLUSIONS

This master's thesis has examined the effect of sensitization on the stress corrosion cracking behavior of marine grade aluminum alloys (Al-Mg). Aluminum alloy 5456-H116 double cantilever beam (DCB) and single edge notch beam (SENB) samples were sensitized at 175°C for varying durations of time and then mechanically tested in salt water. The effect of sensitization was investigated through crack growth rate measurements on statically loaded samples subjected to 3.5 wt% NaCl (salt water). Microstructural and micromechanical tests were performed to characterize the effects of sensitization on the microstructure of the material, and mass loss tests quantified the degree of sensitization (DOS). DCB testing was successfully used to measure K_{ISCC} and crack velocity plateaus for sensitized material. Corrosion fatigue testing in salt water was attempted to determine the threshold stress intensity of the material but was unsuccessful.

Sensitization increased as time at temperature increased with little difference in mass losses above 336 hours. Mass losses in AA5456-H116 are higher at shorter aging times than AA5083-H131 indicating that AA5456 has a much greater susceptibility to IGSCC after sensitization. Crack growth rate results showed that plateau crack velocity ranges increased as sensitization increased and the stress intensity range decreased as sensitization increased. Compared to AA5083, the trends in these values are similar; however, differences in testing geometry and temper make a direct comparison between the two materials difficult.

The fracture surfaces of the AA5456-H116 samples showed a marked difference between the fatigue pre-crack and SCC regions. Stress corrosion fracture surfaces did not exhibit a planar crack front but instead showed extensive secondary cracks that extended in three dimensions throughout the SCC region. This work suggests that sensitized AA5456 readily stress corrosion cracks after minimal sensitization time but may show improved stress corrosion cracking characteristics compared to AA5083, depending upon the temper of the alloy. The effects of sensitization on corrosion fatigue behavior require further study.

THIS PAGE INTENTIONALLY LEFT BLANK

LIST OF REFERENCES

- [1] ASM International, "Standard specification for high magnesium aluminum-alloy sheet and plate for marine service and similiar environments," vol. B928/B928M, ed, 2009.
- [2] M. Skillingberg. (2004). *The aluminum industry continues support for the marine market new temper definitions published.* Available: <http://www.aluminum.org/Content/NavigationMenu/TheIndustry/IndustryStandards/TheAluminumIndustryContinuesEffortstoSupporttheMar.pdf>
- [3] M. G. Fontana, "Stress corrosion," in *Corrosion Engineering*, third ed Singapore: Mc Graw Hill Book Co., 1987, pp. 109–142.
- [4] J. E. Hatch, *Aluminum: Properties and Physical Metallurgy*. Metals Park, OH: ASM International, 1984.
- [5] R. Schwarting et al. "Manufacturing techniques and process challenged with CG47 class ship aluminum superstructures modernization and repairs," in *Fleet Maintenance & Modernization Symposium 2001: Assessing Current & Future Maintenance Strategies*, San Diego, 2011.
- [6] ASM International. (2012, May 30). *Alloy Phase Diagrams Center*. Available: <http://www1.asminternational.org.libproxy.nps.edu/asmenterprise/apd/default.aspx>
- [7] H. Bushfield and M. Cruder, "Sensitized marine aluminum plate & ASTM standard specification B928-an update," in *SNAME Section Meeting*, 2006.
- [8] ASM International, "Standard specification for aluminum and aluminum-alloy sheet and plate," vol. B209, ed, 2010, p. 26.
- [9] ASM International, "Standard test method for determining the susceptibility to intergranular corrosion of 5XXX series aluminum alloys by mass loss after exposure to nitric acid," vol. G67-04, ed: ASTM International, 2004, pp. 1–3.
- [10] E. Herzberg, "The annual cosst of corrosion for DOD," presented at the DOD Corrosion Conference, McLean, VA, 2009.
- [11] J. Kaufman, *Introduction to Aluminum Alloys and Tempers*. Materials Park, OH: ASM International, 2000.
- [12] R. Holtz et al. "Corrosion fatigue of Al 5083-H131 sensitized at 70,100, and 175°C relation to microstructure & degree of sensitization," in *DoD Corrosion Conference*, La Quinta, CA, 2011.

- [13] F. S. Bovard et al. "Relevance of standardized tests and development of sensitization resistant 5XXX products," in *Workshop on Sensitization of Aluminum Alloy 5XXX Series*, 2011.
- [14] J. K. Brosi and J. J. Lewandowski, "Delamination of a sensitized commercial Al-Mg alloy during fatigue crack growth," *Scripta Materialia*, pp. 799-802, 2010.
- [15] C. Menzemer and T. S. Srivatsan, "The effect of environment on fatigue crack growth behavior of aluminum alloy 5456," *Materials Science and Engineering* vol. A271, pp. 188–195, 1999.
- [16] C. B. Crane and R. P. Gangloff, "Stress corrosion cracking of low temperature sensitized AA5083," University of Virginia, Charlottesville, Va.
- [17] J. L. Searles et al. "Stress corrosion cracking of sensitized AA5083 (Al-4.5Mg-1.0Mn)," *Aluminum Alloys 2002: Their Physical And Mechanical Properties Pts 1–3*, vol. 396–4, pp. 1437–1442, 2002.
- [18] R. Goswami et al. "Precipitation behavior of the beta phase in Al-5083," *Materials Science And Engineering A-Structural Materials Properties Microstructure And Processing*, vol. 527, pp. 1089–1095, 2010.
- [19] I. N. Oguocha et al. "Effect of sensitization heat treatment on properties of Al-Mg alloy AA5083-H116," *Journal Of Materials Science*, vol. 43, pp. 4208–4214, 2008.
- [20] F. S. Bovard, "Sensitization and environmental cracking of 5XXX aluminum marine sheet and plate alloys," in *Corrosion in Marine and Saltwater Environments*, T. T. D. A. Shifler, Ed., ed Pennington, NJ: The Electrochemical Society, Inc., 2005.
- [21] R. Kelly et al. "Development and validation of an integrated intergranular corrosion/cracking model of Al-Mg alloys for naval applications," in *Workshop on Sensitization of Aluminum Alloy 5XXX Series*, 2011.
- [22] J. C. Farmer and S. Menon, "General corrosion, localized corrosion, and environmental cracking of modern engineering materials," *Encyclopedia of Life Support Systems*, 2011.
- [23] S. Benedictus-deVries et al. "Fatigue crack initiation behavior of welded AA5083 in a seawater environment," *Journal of Engineering Materials and Technology*, vol. 126, pp. 199–203, 2004.
- [24] N. Birbilis and R. Buchheit, "Electrochemical characteristics of intermetallic phases in aluminum alloys - An experimental survey and discussion," *Journal of Electrochemistry Society*, vol. 152, pp. B140-B151, 2005.

- [25] R. H. Jones et al. "Crack-partial interactions during intergranular stress corrosion of AA5083 as observed by cross-section transmission electron microscopy," *Scripta Materialia*, vol. 50, pp. 1355–1359, 2004.
- [26] R. H. Jones et al. "Stress corrosion cracking of Al-Mg and Mg-Al alloys," *Corrosion Science Section*, vol. 60, pp. 1144–1154, 2004.
- [27] M. Pourbaix, *Atlas of Electrochemical Equilibria in Aqueous Solutions*. Houston, TX: NACE, 1974.
- [28] R. H. Jones and R. E. Ricker, "Stress corrosion cracking," in *Stress Corrosion Cracking, Materials Performance and Evaluation*, ed Materials Park, OH: ASM International, 1992, p. 1.
- [29] J. C. Farmer, "Stress Corrosion Cracking," in *MS3202 Lecture 13*, J. C. Farmer, Ed., ed. Naval Post Graduate School Monterey, CA, 2012.
- [30] R. H. Jones, "Stress-corrosion cracking," in *ASM Handbook*. vol. 13A, A. I. H. Committee, Ed., ed Ohio: ASM International, 2010, pp. 346–366.
- [31] W. D. Callister, *Materials Science and Engineering: An Introduction*. York, PA: John Wiley and Sons, Inc., 2007.
- [32] B. J. Banazwski, "Using x-ray diffraction to assess residual stresses in laser peened and welded aluminum," M.S. thesis, Dept. Mech and Aero. Eng., Naval Post Graduate School, Monterey, CA, 2011.
- [33] A. J. McEvily, "Fatigue crack thresholds," in *ASM Handbook*. vol. 19, A. I. H. Committee, Ed., ed Ohio: ASM International, 2010, pp. 134–152.
- [34] P. L. Anderson, "Corrosion fatigue testing," in *ASM Handbook*. vol. 19, A. I. H. Committee, Ed., ed Ohio: ASM International, 2010, pp. 193–209.
- [35] K. N. Tran et al. "Laser shock peening improves fatigue life of lightweight alloys," *Welding Journal*, vol. 85, pp. 28–31, 2006.
- [36] O. Hatamleh, "A comprehensive investigation on the effects of laser and shot peening on fatigue crack growth in friction stir welded AA 2195 joints," *International Journal of Fatigue*, vol. 31, pp. 974–988, 2009.
- [37] N. Sidhom et al. "Fatigue strength improvement of 5083 H11 Al-alloy T-welded joints by shot peening: experimental characterization and predictive approach," *International Journal of Fatigue*, vol. 27, pp. 729–745, 2005.
- [38] F. Zucchi et al. "Pitting and stress corrosion cracking resistance of friction stir welded AA 5083," *Materials And Corrosion-Werkstoffe Und Korrosion*, vol. 52, pp. 853–859, 2001.

- [39] J. C. Park and S. J. Kim, "Electrochemical properties in a seawater environment of 5456-H116 aluminum alloy subjected to optimal friction stir processing," *Physica Scripta*, vol. T139, p. 5, 2010.
- [40] H. R. Mattern, "Laser peening for mitigation of stress corrosion cracking at welds in marine aluminum," M.S. thesis, Dept. Mech and Aero. Eng, Naval Post Graduate School, Monterey, CA, 2011.
- [41] C. S. Montross et al. "Laser shock processing and its effects on microstructure and properties of metal alloys: a review," *International Journal of Fatigue*, vol. 24, 2002.
- [42] ASM International, "Standard practice for making and using precracked double beam stress corrosion specimens," vol. G168, ed. Pennsylvania: ASTM International, 2006.
- [43] ASM International, "Standard test method for linear-elastic plane-strain fracture toughness K_{IC} of metallic materials," vol. E399-09, ed. Pennsylvania: ASTM International, 2009.
- [44] C. Wong, "Causes of failure in aluminum ship structures," in *Aluminum alloy 5xxx series workshop*, 2011.

INITIAL DISTRIBUTION LIST

1. Defense Technical Information Center
Ft. Belvoir, Virginia
2. Dudley Knox Library
Naval Postgraduate School
Monterey, California
3. MAE Department Chairman,
Dr. Knox Millsaps
Naval Postgraduate School
Monterey, California
4. Engineering and Technology Curricular Office, Code 34
Naval Post Graduate School
Monterey, California
5. Professor Luke N. Brewer
Naval Postgraduate School
Monterey, California
6. Dr. Joseph C. Farmer
Directorate Senior Scientist
National Ignition Facility & Photon Sciences
Lawrence Livermore National Laboratory (LLNL)
Livermore, California